LIVERPOOL JOHN MOORES UNIVERSITY

LJMU Research Online

Liu, Q, Miao, W, Bashir, M, Xu, Z, Yu, N, Luo, S and Li, C

Aerodynamic and aeroacoustic performance assessment of a vertical axis wind turbine by synergistic effect of blowing and suction

http://researchonline.ljmu.ac.uk/id/eprint/17773/

Article

Citation (please note it is advisable to refer to the publisher's version if you intend to cite from this work)

Liu, Q, Miao, W, Bashir, M, Xu, Z, Yu, N, Luo, S and Li, C (2022) Aerodynamic and aeroacoustic performance assessment of a vertical axis wind turbine by synergistic effect of blowing and suction. Energy Conversion and Management. 271. ISSN 0196-8904

LJMU has developed **LJMU Research Online** for users to access the research output of the University more effectively. Copyright © and Moral Rights for the papers on this site are retained by the individual authors and/or other copyright owners. Users may download and/or print one copy of any article(s) in LJMU Research Online to facilitate their private study or for non-commercial research. You may not engage in further distribution of the material or use it for any profit-making activities or any commercial gain.

The version presented here may differ from the published version or from the version of the record. Please see the repository URL above for details on accessing the published version and note that access may require a subscription.

For more information please contact researchonline@ljmu.ac.uk

http://researchonline.ljmu.ac.uk/

Aerodynamic and aeroacoustic performance assessment of a vertical axis wind turbine by synergistic effect of blowing and suction

Qingsong Liu[a], Weipao Miao[a, b, *], Musa Bashir [c], Zifei Xu [c], Nanting Yu[d], Shuai Luo[a], Chun Li[a b]

[a] *School of Energy and Power Engineering, University of Shanghai for Science and Technology, Shanghai, 200093. China*

[b] *Shanghai Key Laboratory of Multiphase Flow and Heat Transfer in Power Engineering, Shanghai 200093, China*

[c] *Liverpool Logistics, Offshore and Marine (LOOM) Research Institute, Liverpool John Moores University, Liverpool, Byrom Street, L3 3AF, UK*

[d] *School of Engineering, Computing and Mathematics (SECaM), University of Plymouth, Plymouth, PL48 AA, UK*

Abstract

The power efficiency of Darrieus wind turbines significantly deteriorates during rotation caused by periodic dynamic stall at low tip speed ratios. This leads to a strong fluctuation in torque and a reduction in energy acquisition. This paper aims to improve the aerodynamic performance of an H-type Darrieus wind turbine using an innovative fluidic flow control technique based on the synergistic effect of blowing and suction. The aeroacoustic noise emissions accomplished with this enhancement are evaluated. The Improved Delayed Detached Eddy Simulation turbulence model and the Ffowcs Williams-Hawkings acoustic analogy method are adopted to simulate the instantaneous flow field and predict the far field noise. Following validation of the numerical approach using wind tunnel experimental data on a static airfoil, an orthogonal experimental design method was used to analyze and optimize the operating factors. The factors include suction position relative to leading-edge (L_s), blowing position relative to trailing-edge (L_b) and jet coefficient (C_μ). The results indicate that C_μ plays crucial role in determining the airfoil performance, while the role of L_b is almost negligible. Furthermore, the impact of optimal combination of these factors was analyzed based on three different control strategies. It is found that appropriate application of the active control solution can eliminate the wind turbine's negative torque, avoid excessive alternating load on the rotor and improve the energy extraction efficiency. The aeroacoustic noise estimation shows that the active device can reduce the noise emission by moderating pressure fluctuation, stabilizing the flow field and influencing the vortex shedding. Similarly, the proposed active control solution can reduce the wind turbine noise level by up to 6.56 dB by modifying the sound pressure spectra at frequencies between 100 and 1000 Hz.

Keywords: Vertical axis wind turbine, Active flow control, Aerodynamic, Aeroacoustic, Computational fluid dynamics, Noise.

Nomenclature

Acronyms

2-D	Two-dimensional
3-D	Three-dimensional
AFC	Active flow control
AFM	Aerodynamic Figure of Merit
AOA	Angle of Attack
BEM	Blade Element Momentum
BL	Boundary Layer
BSS	Blowing-Suction Synergy
CC	Circulation Control
CFD	Computational Fluid Dynamics
CFJ	Co-Flow Jet
DBD	Dielectric Barrier Discharge
DES	Delayed Detached Eddy Simulation
FWH	Ffowcs Williams - Hawkings (acoustic analogy method)
GF	Gurney Flap
HAWT	Horizontal-Axis Wind Turbine
IDDES	Improved Delayed Detached Eddy Simulation
JF	Jet Flap
LDR	Lift-to-Drag Ratio
LES	Large Eddy Simulation
OED	Orthogonal Experimental Design
OSPL	Overall Sound Pressure Level
NACA	National Advisory Committee for Aeronautics

Symbols

B_{in}	Blowing in inner side of blades [-]
B_{out}	Blowing in outside of blades [-]
C_μ	Jet coefficient [-]
C_L	Lift Coefficient [-]
C_D	Drag Coefficient [-]
c	Chord Length [m]
c_p	Specific heat capacity at constant pressure [J/(kg·K)]
C_P	Power Coefficient [-]
H	Blade Height [m]
Gi	Number of Grids [-]
L_b	Position of blowing slot [m]
L_s	Position of suction slot [m]
η	Efficiency of the air pump [-]
N	Number of Blades [-]
P_{BSS}	The power consumed by BSS [W]
P	Power Output [W]
$p_{rms'}$	Effective sound pressure [Pa]
ρ	Air Density [kg/m^3]
p_{ref}	Reference acoustic pressure [Pa]
R	Rotor Radius [m]
Re	Reynolds Number [-]
S_{in}	Suction in inner side of blades [-]
S_{out}	Suction in ouside of blades [-]

NREL	National Renewable Energy Laboratory	T_{ij}	Lighthill stress tensor [-]
PA	Plasma Acuator	V_∞	Incoming Velocity [m/s]
PFC	Passive flow control	V_b	Velocity of blowing [m]
RANS	Reynolds-averaged Navier-Stokes	V_s	Velocity of suction [m]
SB	Straight-bladed	W_b	Width of blowing slot [m]
SJ	Synthetic Jet	W_s	Width of suction slot [m]
SST	Shear Stress Transport	ω	Rotational Speed [rad/s]
SPL	Sound Pressure Level	μ	Dynamic Viscosity [Pa·s]
TSR	Tip-speed ratios	$y+$	Dimensionless Wall Distance [-]
URANS	Unsteady Reynolds-averaged Navier-Stokes	σ	Solidity of Rotor [-]
VAWT	Vertical-Axis Wind Turbine	θ	Azimuth Angle [°]

1. Introduction

Wind energy is rapidly developing worldwide due to its non-polluting and renewable advantages, making it an important clean energy source [1]. As one of the mainstream devices for wind energy utilization, Vertical-Axis Wind Turbine (VAWT) is a device of choice for wind energy extraction in marine and urban areas [2]. VAWT is made of a simple structure and has advantages of scalability, more eco-friendliness, and low manufacturing and maintenance costs compared to Horizontal-Axis Wind Turbine (HAWT). However, the flow field of VAWT is extremely complex due to dynamic stall, wake interactions and rotational effects. These effects have adverse consequence on aerodynamic efficiency and lifetime of the wind turbine [3]. Furthermore, the noise pollution generated by the VAWT in operation, especially the aerodynamic noise, has a negatively impact on human beings, and both aquatic and terrestrial ecosystems. This greatly impedes the rapid development of VAWTs and urgently requires robust mitigating measures. Consequently, further studies are needed to simulate and evaluate VAWT's aerodynamic and aeroacoustic performance to overcome its limitations.

In recent decades, Computational Fluid Dynamics (CFD) methods have been extensively used to simulate the aerodynamics of wind turbines. This is because it can effectively obtain detailed flow field information. Since the principles of noise generation and propagation are governed by the conservation laws of fluid dynamics, the CFD approach is also widely used to study the aeroacoustic noise sources problems, with the noise propagation to the far-field calculated using the Ffowcs Williams - Hawkings (FW-H) equation.

For numerical simulations using CFD methods, the modeling of turbulence is crucial to obtaining the accuracy of computational results. It has been proven that the Shear Stress Transport (SST) k-ω model based on the Reynolds-averaged Navier-Stokes (RANS) method is suitable for evaluating the aerodynamic performance of wind turbines in respect to computational efficiency and accuracy [4]. For the noise predication, Tadamasa and Zangeneh [5] calculated different types of noise radiated from the NREL Phase VI wind turbine. The RANS approach-based SST k-ω model were used to calculate the flow field variables and FW-H codes were used to predict the noise emission. Mohamed [6] investigated the solidity, blade shape, and TSR effects on the aeroacoustic noise of H-type VAWT based on two-dimensional (2-D) unsteady RANS (URANS) model. However, the traditional RANS turbulence model with inherent time-averaged properties has limitations in accurate prediction of highly unsteady features and this renders the direct acoustic predictions from RANS questionable. Using the Large Eddy Simulation (LES) method shows superiorities to RANS, but the relatively high computational cost of simulating high Reynolds number and its limitations in industrial applications undermines its broader utilization.

The Detached Eddy Simulation (DES), including the delayed DES (DDES) and improved delayed DES (IDDES) methods, is a hybrid modeling approach that combines features of RANS and LES methods. The approach can provide detailed and accurate solutions for the flow field around a wind turbine. Amgad et al. [7] compared the RANS and the DDES models to predict the aerodynamic and aeroacoustic performance of a VAWT. Their study proved that the DDES model can produce good agreement over the whole TSR range, while URANS can be accepted only at the low TSR. Benim et al. [8] used IDDES to calculate the aerodynamic and noise characteristics of a small HAWT and verified the accuracy of the calculation procedure with experimental

data. The predicted aerodynamic efficiency deviation is within a reasonable and allowable range. The calculated sound pressure level is measured as only 5.9% higher than the experimental value. After that, Su et al. [9] adopted similar methods for an assessment analysis of aeroacoustics of VAWT. The model was validated by comparing the power coefficients with experimental values at different TSR. In this way, using the IDDES model combined with FW-H analogy for simulating and evaluating the wind turbine performance is deemed appropriate.

Since the noise radiation pattern is determined by the pressure fluctuation arising from the interaction of the VAWT blades with their surrounding turbulence, this causes aerodynamic acoustics to be closely related to the aerodynamic behavior. Accordingly, improving the aerodynamic performance automatically reduces the noise radiation [8]. Therefore, the exploration of effective and innovative practical flow control methods for improving the aerodynamic performance of the VAWT becomes necessary.

The flow control method is normally divided into active flow control (AFC) and passive flow control (PFC). PFC has advantages of requiring no external energy input and control system, being made of simple structure, low cost and easy implementation. Its geometric mechanisms are usually added to the blade surface to change its aerodynamic shape. Examples of PFC include vortex generator [10], trailing edge flap [11], leading edge slat [12] and Gurney flap (GF) [13]. Although PFC has many benefits, it has a narrow adaptation range and poor regulation performance. In comparison, AFC can improve the local or even global flow field structure through a small range of external energy input. This can effectively reduce the aerodynamic loss caused by flow separation, making it suitable for flow regime control under multiple working conditions. Common AFC methods include Boundary layer (BL) suction, jet flap, synthetic jets, Co-flow jet (CFJ), plasma actuator, circulation control variable pitch control and flexible trailing edge flap. Most of these technologies have been investigated in different fields, such as aviation (aircraft & helicopters), automobiles, and wind turbines.

However, it is important to note that for VAWTs, their frequent switching between pressure and suction sides, long operating cycles [14] and high rotational speed means they require a much higher response frequency for AFC. In ability of VAWT to meet these requirements may result in mechanical-based variable pitch control and trailing edge flap being more prone to failure. Therefore, the fluidic flow control strategies may be more suitable to VAWTs.

1.1. Overview of fluidic flow control strategies

In this section, an overview of AFC technologies currently applied to wings or blades that are worthy of application in VAWTs is presented.

1.1.1. BL suction

The concept of BL suction was introduced by Prandtl et al. [15] to inhibit the flow separation on a cylinder surface. Subsequent studies have concentrated on developing applications for airfoils and wind turbines. A typical BL suction mechanism is shown in Fig. 1. The exhausted BL is removed by a suction slot on the suction side of the airfoil to create a fresh, high-energy BL. This inhibits the formation and development of separation vortices, which eventually produces higher lift [16].

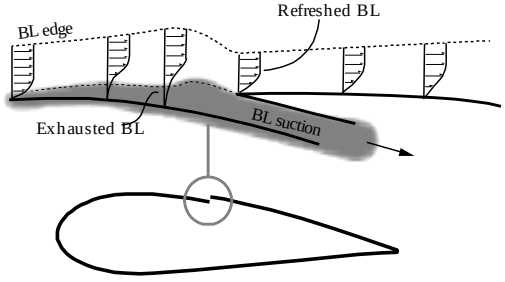

Fig. 1 Schematic of BL Suction (Pechlivanoglou et al. [17])

Abdullah et al. [18] experimentally studied continuous normal suction on the aerodynamic performance of the NACA 0015 airfoil and consider the impact of suction slot location and the suction strength. Their results show that a suction control with higher mass flow rate significantly increases the lift-to-drag ratio but also increases the drag coefficient. More importantly, the extra power consumed by this active device was not considered. To evaluate the economics of this active control, Lei et al. [19] numerically investigated the effect of BL suction on a NACA 2415 airfoil. It was concluded that the suction control should be used with high angle of attack (AOA), and the suction speed should be as low as possible to reduce the energy consumption subject to the lift-to-drag ratio (LDR) meeting the aerodynamic requirements.

Suction techniques have been proven to be effective in enhancing the airfoil performance, but the principle of suction effect in VAWTs is not yet fully elaborated. Rezaeiha et al. [20] employed BL suction on a single bladed VAWT to control flow separation and improve turbine efficiency. Promising results were obtained at tip-speed ratio (TSR) of 2.5, 3.0 and 3.5, with a corresponding improvement in power coefficients by 219.6%, 74.3% and 19.6%. It is found that the optimal suction location is most sensitive to Reynolds number, less affected by turbulence intensity, and least affected by TSR. These results were based on a single blade, which may not suitably translate to predictions for the actual flow conditions of a multi-blade VAWT. Following this, Sun et al. [21] studied the effects of BL suction on a three bladed VAWT and indicated that multi-suction slots could achieve higher power efficiency at low and high TSRs compared with the single suction slot systems. However, the flow mechanism behind their enhancement for power production was not clearly explained. This should be further investigated.

1.1.2. Jet flap

The jet flap (JF) (Fig. 2) is another AFC method, which performs the same function as a conventional GF by changing the trailing edge Kutta conditions. This is achieved by altering the amount of circulation generated by the airfoil to significantly improve the lift with minimal drag cost [22].

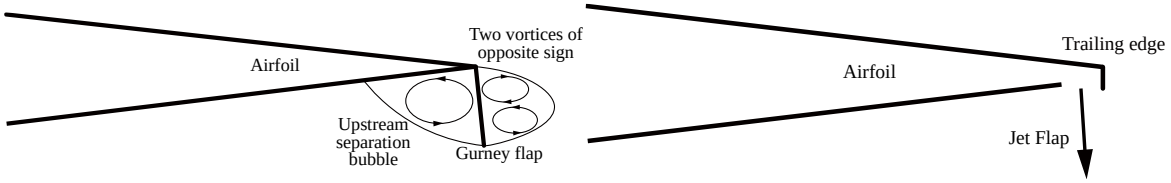

(a) GF (b) Jet flap

Fig. 2 Schematic of Gurney and its virtual type (Feng et al. [24])

Agarwal et al. [23] configured a test wing with GF and JF to study the combined effects. The study found that using the trailing edge jet was an efficient way to further increase the lift coefficient. Feng et al. [24] proposed a novel plasma GF concept for the NACA0012 airfoil, which achieves the function of JF using plasma actuators. It was found that the plasma JF can increase the Airfoil maximum lift coefficient by 7.5% and significantly improves the LDR ratio even at a small AOA. However, it is found that both methods changed the shape of the airfoil and may introduce some structural drag. Furthermore, the jet parameters were defined as a single operating condition, while other geometric parameters affecting the performance of the JF were not explored in detail. Fu et al [25] placed the JF on the airfoil pressure side without changing the airfoil aerodynamic shape to investigate the impacts of the critical parameters of jet angle, position and momentum coefficient on the aerodynamic performance of the NACA0012 airfoil. The results show that placing the jet closer to the trailing edge increases the lift and lowers the drag. When positioned at the leading edge, moving forward from 0.98 chord length, the increase in momentum coefficient increases the drag. Following determination of all jet flap parameters, an optimal jet angle that will further increase the lift was identified. Du

et al. [26] and Jian et al [27] have recently employed the JF on a compressor airfoil to increase the wall-attachment effect and mitigate the secondary flow losses. This approach eventually improves the aerodynamic performance of the compressors.

The current JF has better active control ability and low equipment drag, making it a very attractive to lift enhancement technology for aeronautical applications. Consequently, the JF shows great potential to displace the mechanical GF in some applications. However, the Jet flap has a significant challenge in mitigating the dynamic stalls effects on VAWTs. This explains the low uptake of the technology in VAWT as attested by its near total absence of any mention in the relevant literatures.

1.1.3. Synthetic jet

The synthetic jet (SJ) strategy (Fig. 3) works mainly via a piezoelectric brake, which generates continuous suction and blowing by vibrating the membrane periodically [28].

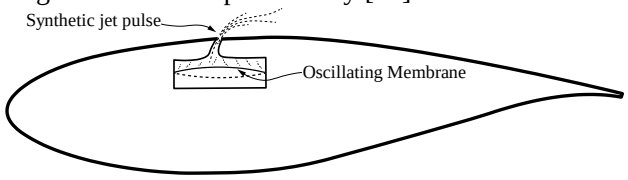

Fig. 3 Schematic of Synthetic jet (Pechlivanoglou et al. [17])

Yen et al. [29] conducted an experimental study of an SJ arranged on an oscillating NACA0020 airfoil. This active control method can potentially enhance turbine performance and reduce the low TSR noise emission of the VAWT relative to the baseline configuration. Menon et al. [30] numerically evaluated the impacts of different SJ parameters on the aerodynamic performance of a three-blade VAWT. The study found that the average axial force can be increased by 12% at a reduced frequency of 5 Hz and a blowing ratio of 1.5. However, the energy consumption required for SJ was not mentioned. It should be noted that using SJ requires external energy, and the direct application of the traditional SJ method to VAWT may not be suitable where energy consumption is high [31]. Wang et al. [32] recently proposed three different trailing edge SJ for SB VAWT. The juxtaposition-type SJ is better than the other two configuration and can effectively avoid the vibrating membrane failure problem arising from the large pressure difference between the inner and outer sides of the blade. Intermittent blowing and suction has been proposed as a route to significant energy saving. However, the inherent aerodynamic deficiency of a SJ is its inability to produce strong jets due to the tiny displacement of the vibrating membrane. In addition, lack of precise control makes it difficult for SJ to achieve an improved effect for the global flow field. Therefore, this needs to be carefully considered if they are to be employed in VAWT.

1.1.4. Plasma actuators

The plasma actuator (PA) is a relatively novel approach for flow control in recent years. The main PA mechanism generates plasma wind by heating or accelerating the air near the actuator using a high-power discharge. This modifies the BL distribution and effectively suppresses flow separation [33]. Among the various PA, the Dielectric Barrier Discharge (DBD) (Fig. 4) based PA offers good control ability for low-speed fluid. As it has a simple structure, no moving parts, fast response speed and light weight, this approach has been receiving attention from researchers.

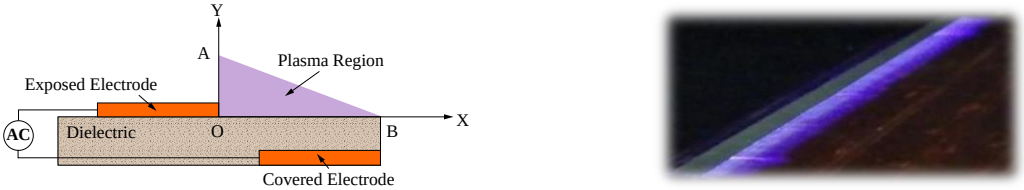

(a) Schematic of Plasma actuator (b) Plasma produced by actuator

Fig. 4 Schematic of Plasma actuator and visualization of the actuator effect (Ma et al. [36])

Greenblatt et al. [34] experimentally studied the impacts of DBD PA on the aerodynamic performance of small high-solidity VAWT. The DBD PA is mounted on the leading-edge of a turbine blade and operates only in the upwind region to inhibit flow separation. Performance benefits in the downwind region have not been explored in detail. Greenblatt et al. [35] implemented switching DBD PA on the inner and outer sides of the VAWT blades for simultaneous excitation in both the upwind and downwind regions. Dynamic stall could be significantly suppressed with dual-side excitation leading to consistently larger performance increase than for single-side excitation. More recently, Ma et al [36] numerically investigated the impacts of DBD PA on a H-type VAWT. Eight active control strategies were proposed to distinguish the excitation azimuth range after a detailed analysis of the dynamic stall characteristics of the VAWT. It was found that DBD PA can effectively improve the power extraction of wind turbine and work well when the azimuth angle is within the range of 60° to 120°.

Application of these principles in flow control of wind turbines is currently under extensive investigation. The main benefit of the PA approach is they do not require inserted units and can be easily integrated into the wind turbine blades by simple adhesion. As with the SJ, DBD PA does not require additional air sources, thus reducing the complexity of the system. However, this active device is very sensitive to Reynolds number variations and is unsuitable for high Reynolds number conditions. On the other hand, the plasma-induced jet increases the BL momentum and can easily cause flow instabilities, so a suitable installation location needs to be identified when used in VAWT with frequent changes in AOA.

1.1.5. Circulation control

The motivation for Circulation Control (CC) (Fig. 5a) is based on the well-known Coanda effect, which increases the flow reattachment capability by a fast blown flow along a highly curved surface and diverting the jet without separation [37]. It should be noted that CC, unlike JF, improves lift mainly by changing the stagnant streamline movement and increasing circulation around the blunt body.

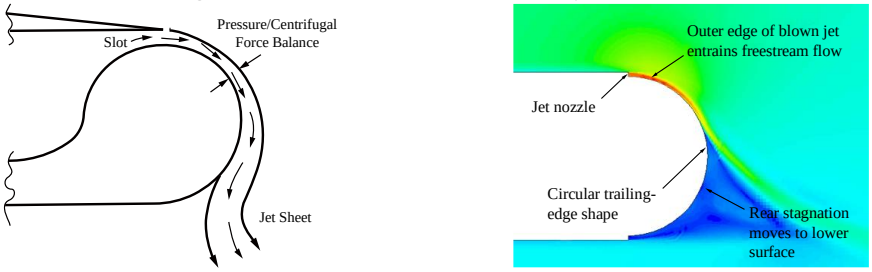

(a) Basics of Circulation Control Aerodynamics (Jones et al. [38])

(b) Velocity contours of circulation control (Shires et al. [40])

Fig. 5 The principle of the circulation control and its application

Graham et al. [39] modified the NACA0018 airfoil shape to achieve the CC control, then numerically investigated the CC effects over two Reynolds numbers and a wide range of AOA. Constant CC control leads to a decrease in LDR before the occurrence of a stall, which may deteriorate the performance of the VAWT. Shires et al. [40] numerically investigated the aerodynamic performance of different CC airfoils (Fig. 5b) and then used a blade element momentum (BEM) based model to evaluate the performance of a VAWT rotor with these CC airfoils to consider the feasibility of the technology. For moderate momentum coefficients, a net power increase could be achieved albeit not significantly higher than that of a baseline VAWT. However, the airfoil shape used in the Shires et al. [40] study was simple and not optimized for the application. Previous CC control studies have generally changed the airfoil shape to a blunt trailing edge with a large curvature. This severely affects the original solidity requirements of the VAWT and thus results in the original rated power of the wind turbine not being met. More numerical and experimental studies are needed to verify the feasibility of CC implementation on a VAWT.

1.1.6. Co-flow jet

The concept of CFJ (Fig. 6) was first proposed by Dano et al. [41]. to control the flow separation of a static airfoil. There are two similar slots on the suction side of the airfoil. The slot on the leading edge blowing tangentially along the wall while the slot on the trailing edge suction having equal amount of flow. In comparison to conventional blowing-based jets, the CFJ does not require extra air source and only requires an air pump for it to achieve better flow control.

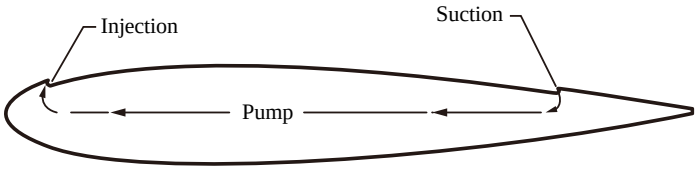

Fig. 6 Schematic of CFJ concept (Sun et al. [44])

Xu et al. [42] numerically investigated the effects of CFJ on the dynamic stall characteristics of an S809 airfoil. CFJ can reduce the scale and range of vortex shedding at large AOA and mitigate the load fluctuations to significantly suppress the dynamic stall. Power consumption analysis shows good economics for CFJ. Using the traditional CFJ method, Liu et al. [43] proposed a CFJ-sloping slot with the same airfoil profile as the baseline airfoil between the injection and suction slots, but with the shape around the slot changed. The modified CFJ was more effective in suppressing shock-induced dynamic stall of the SC1095 airfoil than the conventional CFJ, especially at high AOA and low-speed conditions. However, the required power consumption was not considered behind the improvement. To further save energy expenditure for this active device, Sun et al [44] first proposed an intermittent CFJ injection strategy and applied it to a three-bladed VAWT to investigate the control effects of different CFJ parameters. CFJ can greatly improve the aerodynamic efficiency and reduce the energy consumption of the VAWT by alternating excitation on both sides of a blade surface. However, the jet passage changes the aerodynamic shape of the airfoil, which may cause some negative effects at higher TSR. This means that the geometric parameters of CFJ need further optimization when applied to a VAWT.

1.2. Research gap and motivation

Following the limitations identified in the above studies, the motivation for this research is to investigate the following aspects to improve the aerodynamic and aeroacoustic performance of VAWT:

(a) Injecting high-energy fluid into the BL to enhance the mixing of free-stream and near-wall flow so that the BL fluid has enough momentum to overcome the inverse pressure gradient, thereby inhibiting or slowing down the BL separation.

(b) Removing the low momentum fluid to enable fresh high-energy fluid to quickly engage in the BL, thus suppressing the formation and development of leading-edge vortices. This will lead to reduction in the flow loss caused by the aggregation of small vortices into large vortices.

(c) Inducing the fluid direction on the wall to change the Kutta-Joukowsky condition, thus increasing circulation to enhance the velocity on airfoil surface or changing the virtual camber to reduce the effective AOA. This will eventually lead to the reattachment of separated flow.

Traditional fluid-based active control solution (BL suction, JF, CC and blowing-based jet etc.) are generally very energy consuming. The primary reason is that suction needs to consider the exhaust of the inhaled air, while blowing needs an external air source. Furthermore, none of these constant excitation control methods are suitable for application in variable operating conditions, especially for VAWT with inherent AOA periodic variations and dynamic fluctuations in load.

In contrast, both SJ and PA have the advantage of being small and robust in construction, making them easy

to integrate into a wind turbine blade. However, the main drawbacks of SJ are their inability to operate over a large frequency range and lack of precision in control. A well-known limitaion of PA is its sensitivity to the Reynolds number. More specifically, the effectiveness of PA decreases with increase in free flow velocity. Eisele et al. [45] found that the impact of PA on a wind turbine airfoil vanishes at $Re \geq 10^5$. Due to the above limitations, the implementation of SJ and PA technology in aerodynamic applications is very limited.

A potential solution to the above limitation is the use of CFJ, which does not require an extra air source. It has been proven that the alternating control on both sides of VAWT blades gives satisfactory results with lower energy consumption. However, the airflow channel of this control solution is outside the blade and will be disturbed by the separated vortex, especially at a large AOA. Therefore, the option may not achieve the desired effect in practical engineering applications. More importantly, the jet channel changes the aerodynamic shape of the airfoil, which may cause some negative effects.

As previously stated, only few numerical studies have examined the active control ability of VAWT noise using suction or blowing-based jets. Consequently, there is a growing interest in research to investigate these active control solutions to characterize the mechanism of noise reduction in VAWTs.

1.3. Present work

In this study, the BSS active control method is proposed to investigate its combined effects on aerodynamic and aeroacoustic characteristics of VAWT using a high-precision CFD numerical solver. In the BSS technique (Fig. 7), there are two similar slots mounted on the inner side and outer side of the VAWT blade. The slot near the leading edge draws air perpendicular to the blade surface, while an equal amount of flow blows out from the slot close to the trailing edge by using an air pump embedded in the airflow channel of the blade.

A comprehensive literature review has revealed several merits of the proposed BSS concept for fluidic AFC solutions:

1. A BSS can achieve a “double effect” by using: (i) the leading-edge suction to remove low momentum fluid to inhibit the formation and development of separated bubbles, and (ii) the trailing edge blowing to increase the virtual camber and reduce the effective AOA of the airfoil to further enhance the fluid adhesion capability.

2. The BSS concept is relatively simple and does not need an additional air source. The air flow pipeline and air pump are arranged inside the blade. The suction and blowing directions are placed perpendicular to the blade surface so that the jet slot will not change the original profile of the airfoil. This ensures that good aerodynamic performance is achieved under conditions where no stall occurs.

3. The BSS concept extends the VAWT operating conditions by making them insensitive to dynamic variable AOA and guarantees that they are no longer limited to only static airfoil application. Thus better flow control effects can be achieved with lower energy consumption for VAWTs simply by changing the excitation azimuth angle.

Therefore, this study is the first to investigate the effects of BSS on aerodynamic performance and noise characteristics for VAWT. The study aims to address the following unanswered questions that hitherto undermined the application of BSS in VAWTs.

1. Is the proposed BSS applicable to a special complex flow characteristics of VAWT caused by periodic variation of AOA and rapid fluctuation of aerodynamic loads?

2. How does the BSS influence the aerodynamic characteristics of static airfoil and three-bladed rotating VAWT? What is the performance enhancement mechanism of the concept?

3. What kind of BSS control strategy is suitable for VAWT, and what are the key factors to be considered in practical engineering application?

4. Does the power generated by the BSS cover the energy consumption it produces? This is also a critical issue for most of the active control techniques.

5. How does the BSS contribute to low-noise design for VAWT and what is the noise reduction mechanism?

2. Model and Methodology

In this section, the adopted geometric model with BSS control is presented in detail. The computational methods and numerical settings used for the aerodynamic and aeroacoustic simulations are also discussed.

2.1 Model description

In this study, a three-bladed H-type VAWT, which has been vastly exploited in 2-D [46] and 3-D [47] numerical simulation, is adopted to investigate the aerodynamic and aeroacoustic characteristics. The geometric and operational features used are identical to those in Castelli et al. [48] (Table 1).

Following the guidelines of Bianchini et al. [49] and Rezaeiha et al. [50], this research first evaluated the applicability of BSS aerodynamic effects on a static airfoil before investigating the three-bladed rotor. There is lack of information on BSS effects for static airfoil, so various BSS parameters concerning geometrical, location specifications and physical properties are also deeply explored in this study. For consistency, the NACA0021 airfoil is adopted for static calculation, which is also used in the production of straight rotor blades.

Table. 1 Geometrical and operational parameters of the SB-VAWT.

Parameter	Value
Chord length c	0.086 m
Rotation Radius R	0.515 m
Number of blades N	3
Solidity $\sigma=Nc/2R$	0.25
Spoke-blade connection	0.5c
Incoming flow velocity V_∞	9 m/s
Rotational speed ω	24.99-57.50 rad/s
TSR λ	1.43-3.30

Since the referenced VAWT used in this study has a high aspect ratio (h/c = 16.98), its middle plane is minimally affected by the tip effect. Moreover, according to Li et al. [51] and Gosselin et al. [52], the 3-D effect is no longer significant when the turbine height (h) is greater than twice the radius. In this case, h/R of the referenced VAWT is 2.83. More importantly, the main focus of this research is to investigate the impact of BSS control on the middle part of the VAWT rather than the flow fluctuations in the vertical direction. Therefore, the 2-D simulations can achieve comparable results to a 3-D complete rotor. After weighing the computational cost and accuracy, the 2-D numerical model was used for subsequent simulations.

In addition, Rezaeiha et al [53] pointed that the shaft may play a crucial role in determining the final power coefficients, especially when the turbine blades rotate into the downwind region, where shedding vortices of the shaft may cause a sudden drop in the power coefficient of the blades. Therefore, the turbine shaft considered in the present 2-D simulation rotates counterclockwise at the same velocity as the turbine blades.

The corresponding BSS concept used for airfoil and wind rotor is shown in Fig 7. The suction slot is located near the leading edge of the upper surface of the airfoil and the blowing slot is located near the trailing edge of the lower surface. A micro-pump draws in air through the leading-edge suction slot perpendicular to the airfoil wall, and the same mass air is blown out through the trailing edge blowing slot again. The velocity inlet is set up for the suction and blowing slots to achieve the BSS function. The distance between the center of the suction slot and the

leading edge is L_s, and the distance between the center of the blowing slot and the trailing edge is L_b. The suction velocity V_s is equal to the blowing velocity V_b. To simplify the calculation and analysis, the pump and internal pipeline are omitted in the study of BSS airfoil. The jet velocity at the suction and blowing slots is set to a constant value according to a given jet momentum coefficient.

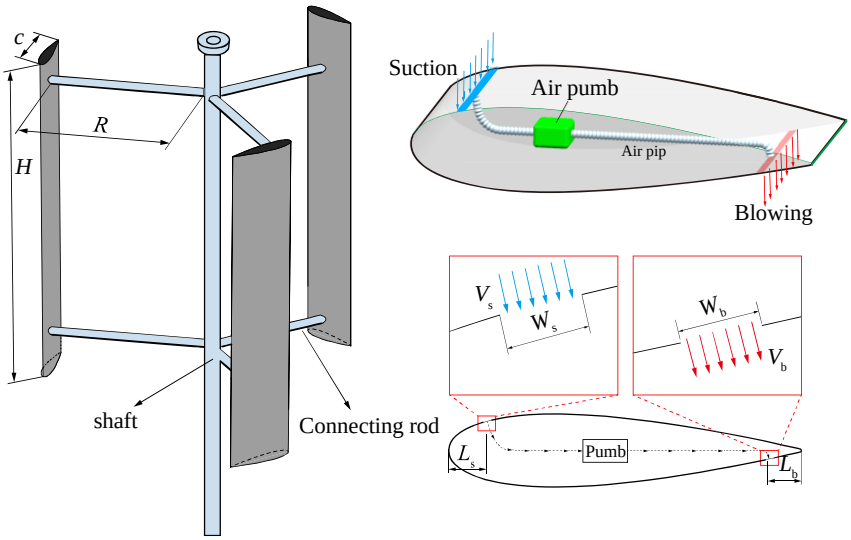

Fig. 7 Geometrical, location specifications and proposed BSS used in static airfoil and VAWT.

For the BSS airfoil, the calculation method for the lift and drag coefficient differs from that of a traditional airfoil because the traditional airfoil is a closed object boundary, and its aerodynamic force is determined by the pressure distribution and the surface friction distribution on the object boundary. The aerodynamic force coefficient of the traditional airfoil can be obtained directly by integrating the pressure coefficient and friction coefficient on the object boundary. However, the surface boundary of BSS airfoil is not closed, and both suction and blow slots are set as the velocity inlet boundary conditions.

Therefore, a closed BSS airfoil boundary needs to be constructed to ensure consistency with the original airfoil profile (Fig. 8). To calculate the aerodynamic forces on the BSS airfoil, the reaction forces of BSS on the airfoil need to be considered.

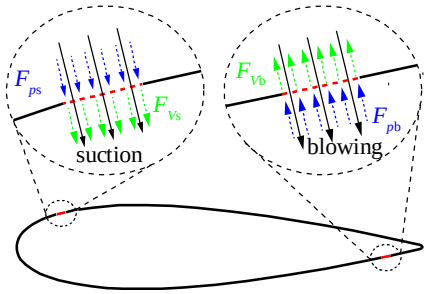

Fig. 8 The reaction forces of BSS. The red dashed lines represent the blowing and suction slot, while the black solid lines represent the direction of BSS. F_{pb} and F_{ps} represent the pressure exerted by blowing and suction, while F_{Vb} and F_{Vs} represent the reaction forces.

Based on the above analysis, the lift and drag coefficients for a BSS airfoil are calculated by Eqs. (1) and (2):

$$C_L = C_{L\_p+\tau} + C_{L\_\mathrm{BSS}} \tag{1}$$

$$C_D = C_{D\_p+\tau} + C_{D\_\mathrm{BSS}} \tag{2}$$

where $C_{L\_p+\tau}$ and $C_{D\_p+\tau}$ are obtained by integrating the surface pressure and shear stress of BSS airfoil. C_{L_BSS} and C_{D_BSS} are the respective BSS reaction coefficients, which can be expressed by Eqs. (3) and (4):

$$C_{L\_\mathrm{BSS}} = \frac{\dot{m}(\vec{V}_\mathrm{s} + \vec{V}_\mathrm{b})}{0.5\rho V_\infty{}^2 \cdot c} \cdot \vec{j} \tag{3}$$

$$C_{D\_\mathrm{BSS}} = \frac{\dot{m}(\vec{V}_\mathrm{s} + \vec{V}_\mathrm{b})}{0.5\rho V_\infty{}^2 \cdot c} \cdot \vec{i} \tag{4}$$

where $\dot{m}$ is the mass flow, kg/s; $\vec{i}$ and $\vec{j}$ are the directional vectors of lift and drag, c is the chord of the airfoil; $\vec{V}_\mathrm{b}$ and $\vec{V}_\mathrm{s}$ are the respective velocity vectors.

The momentum coefficient C_μ is used to measure the jet strength [54], and can be expressed by Eq. (5):

$$C_\mu = 2\dot{m}V_\mathrm{s} / \rho_\infty V_\infty{}^2 c \tag{5}$$

In the BSS concept, the power required to pump the jet is determined by the jet mass flow rate and total pressure ratio required to overcome the total pressure loss of the recirculated jet [43]. which is expressed as Eq. (6):

$$P_\mathrm{BSS} = \dot{m}(H_\mathrm{b} - H_\mathrm{s}) = \frac{\dot{m}c_p \mathrm{T_{ts}}}{\eta} \cdot \left[\left(p_{tb} / p_\mathrm{ts} \right)^{\frac{\gamma-1}{\gamma}} - 1 \right] \tag{6}$$

where H_b and H_s are the total enthalpy of blowing and suction (kJ/kg); c_p for the constant pressure specific heat capacity, taken as $1007\ \mathrm{kJ/(kg \cdot K)}$, $\mathrm{T_{ts}}$ is the total temperature of the suction slot, given as 298.15K (25℃), η is the efficiency of the air pump, taken as 80%; p_{tb} and p_ts is the total pressure of blowing and suction, (Pa), γ for the specific heat ratio, 1.402.

2.2 IDDES turbulence model

The SST $k-\omega$ turbulence model is usually regarded as suitable for simulating the H-type VAWT [55]. Ma et al. [56] and Guo et al. [57] also obtained satisfactory results for power and torque within an allowable error margin. However, the URANS does not capture the small pressure pulses well enough for noise calculations. Therefore, the IDDES model is adopted in this study after verifying its reliability in section 3 and because of the complementary benefits it offers in addressing URANS limitations. The method offers an effective and high-precision solution by providing accurate information for the flow field around the wind turbine [58].

Menter [59] addressed the sensitivity problem of free-stream/inlet conditions and recognized that the ε transport equation (Eq. 7) from the Standard K-Epsilon model could be transformed into an ω transport equation by variable substitution. Menter also introduced a modification to the linear constitutive equation and named the model containing this modification the SST (shear-stress transport) $k-\omega$ model.

$$\frac{\partial}{\partial t}(\rho k) + \nabla \cdot \left(\rho k \bar{\mathbf{v}}\right) = \nabla \cdot \left[\left(\mu + \sigma_k \mu_t\right) \nabla k \right] + P_k - \rho \beta^* f_{\beta^*} \left(\omega k - \omega_0 k_0\right) + S_k \tag{7}$$

where $\overline{\mathbf{V}}$ is the mean velocity, μ is the dynamic viscosity, σ_k is the model coefficient, P_k is a production term, f_{β^*} is the free-shear modification factor, S_k is the user-specified source terms, and k_0 is the ambient turbulence value that counteract turbulence decay.

Based on Shur et al. [60], the IDDES formulation is obtained by replacing the specific dissipation rate ω of transport equation with $\tilde{\omega}$ given in Eq. (8):

$$\tilde{\omega} = \frac{\sqrt{k}}{l_{HYBRID} f_{\beta^*} \beta^*} \tag{8}$$

where f_{β^*} is the free-shear modification factor, β^* is the model coefficients of $k-\omega$ model, and l_{HYBRID} is computed as Eq. (9):

$$l_{HYBRID} = \tilde{f}_d \left(1 + f_e\right) \sqrt{k} / l_{RANS} + \left(1 - \tilde{f}_d\right) C_{DES} \Delta_{IDDES} \tag{9}$$

where $\tilde{f}_d$ is the modified version of the IDDES f_d function, f_e is the elevating function, C_{DES} is the Model Coefficients of $k-\omega$ model, and the Δ_{IDDES} is an altered version of mesh length scale, computed as Eq. (10):

$$\Delta_{IDDES} = \min(\max(0.15d,\ 0.15\Delta,\ \Delta_{\min}),\ \Delta) \tag{10}$$

where $\Delta_{\min}$ is the smallest distance between the cell center under consideration and the cell centers of the neighboring cells.

2.3 Method for calculation of noise

The FW-H acoustics integral formulation is the preferred strategy for far-field noise prediction and has been widely used to calculate wind turbine noise [9]. This model calculates the far-field sound signal radiated from near-field flow data from a CFD solution. The goal is to predict small amplitude acoustic pressure fluctuations at the locations of each receiver.

The FW-H equation is an exact rearrangement of the continuity and the momentum equations into an inhomogeneous wave equation. The FW-H equation gives accurate results even if the surface of integration lies in the nonlinear flow region. The method is based on the free space Green's function to compute the sound pressure at the observer location. The FW-H equation for pressure that is radiated into a medium at rest by a flow in a region or a set of surfaces is defined as Eq. (11):

$$\frac{1}{c_0}\frac{\partial^2 p'}{\partial t^2}-\nabla^2 p'[p'H(f)]=\frac{\partial^2}{\partial x_i \partial x_j}[T_{ij}H(f)]+\frac{\partial}{\partial t}[(\rho_0 v_n+\rho(u_n-v_n)\delta(f)] -\frac{\partial}{\partial x_i}[(P_{ij}n_j+\rho u_i(u_n-v_n)\delta(f)] \tag{11}$$

where the c_0 is the local speed of sound, u_i represents fluid velocity component in the i direction, u_n is the fluid velocity component normal to the surface, v_n is the surface velocity component normal to the surface, ρ is the fluid density, P_{ij} is the compressive stress tensor, $\delta(f)$ is the Dirac Delta function.

The T_{ij} is the Lighthill stress tensor, defined by Eq. (12):

$$T_{ij}=\rho u_i u_j+\sigma_{ij}\left[(p-p_0)-c_0^2(\rho-\rho_0)\right]-\sigma_{ij} \tag{12}$$

where σ_{ij} is the viscous stress tensor.

The left side of Eq. 11 shows the fluctuation operator for calculating pressure fluctuations and the right side shows the noise generation mechanism, in the order of quadrupole (turbulence noise), monopole (thickness noise) and dipole (loading noise) sound sources. Generally, thickness and loading noise are the main noise sources, while the influence of quadrupole noise on tone noise is negligible [9]. Therefore, only the monopole term (define in Eq. 13) and the dipole term (defined in Eq.14) are considered in this paper.

$$\mathrm{p}_T'(\mathbf{x},\,t)=\frac{1}{4\pi}\left(\int_{(f=0)}\left[\frac{\rho_0 v_n\left[(r\dot{M}_r)+a_0(M_r-M^2)\right]}{r^2(1-M_r)^3}\right]dS\right)_{ret} \tag{13}$$

$$\mathrm{p}_L'(\mathbf{x},\,t)=\frac{1}{4\pi a_0}\int_{(f=0)}\left[\frac{\dot{L}_i r_i}{r(1-M_r)^2}\right]dS+\frac{1}{4\pi}\int_{(f=0)}\left[\frac{(L_r-L_i M_i)}{r^2(1-M_r)^2}\right]dS +\frac{1}{4\pi a_0}\int_{(f=0)}\left[\frac{L_r\left[(r\dot{M}_r)+a_0(M_r-M^2)\right]}{r^2(1-M_r)^3}\right]dS \tag{14}$$

where L_i is the blade load vector. $L_i=P_{ij}\cdot n_i+\rho\cdot u_i(u_n-\upsilon_n)$ where $P_{ij}=(p-p_0)\delta_{ij}$, $\dot{L}_i$ is the derivative of the blade load vector with respect to source time, υ_n is the surface normal velocity, r_i is the distance from a source point to the observer, M_r is the Mach number of the source toward the observer. The subscript *ret* indicates retarded time, which is the time of emission.

2.4 Numerical settings

The transient flow field around the static airfoil and VAWT is simulated using the commercial finite volume based CFD package, STAR-CCM+ 15.02.06. Considering the small Mach number and no thermal diffusion, an

incompressible implicit separated flow model is used, and the pressure-velocity coupling is based on the SIMPLE algorithm. The computational convergence is accelerated based on the sub-relaxation factor (which controls the variable updates within each iteration step) property of this algorithm. The second-order upwind scheme is set to compute the convective flux. The turbulence in the transient simulation is modeled using the SST $k-\omega$ based IDDES turbulence model to better capture smaller pressure pulsations for noise calculations, as described in Section 2.2.

The steady-state solution is first calculated based on the RANS equation, and then the time history is cleared to start the unsteady computation. For the static airfoil, several simulations with shorter time steps were performed to compare the average lift coefficients after curve stabilization. The optimal time step (taken as 5×10^{-5} in this paper) was obtained when the lift values were temporally independent or did not vary with decrease in the time steps. For the three-blade VAWT simulations, data sampling starts after 18 revolutions with an azimuthal increment of 0.25° for the wind turbine unsteady simulations, which corresponds to a time step of 0.000175s - 0.0000759 s for different TSR. These values were obtained from the sensitivity analysis described in Section 3.

3. Sensitivity analysis and Validation

The numerical approach used in the subsequent calculations was validated before proceeding to investigate the impacts of BSS control on the Darrieus turbine. The sensitivity analysis and validation work are performed for the NACA0021 static airfoil and the three-bladed VAWT, respectively, as described in sections 3.1 and 3.2.

3.1. NACA0021 Static airfoil

3.1.1. Grid sensitivity analysis

The boundary conditions and grid distribution for the static airfoil are illustrated in Fig. 9. In Fig. 9a, the computational domain is a rectangle of 100*c*×60*c* (reference the work of Kinzel et al. [61]). The computational domain is divided into three sub-domains, where R1 and R2 are grid refinement zone, and R3 is the far-field domain. The numerical simulation under different AOA can be realized by rotating the R1 region. AB is the velocity inlet and CD is the pressure outlet, which are 40*c* and 60*c* from the airfoil center point, respectively, and the incoming flow velocity V_∞ is 15.67 m/s, and the Reynolds number based on the chord length is 1.4×10^5.

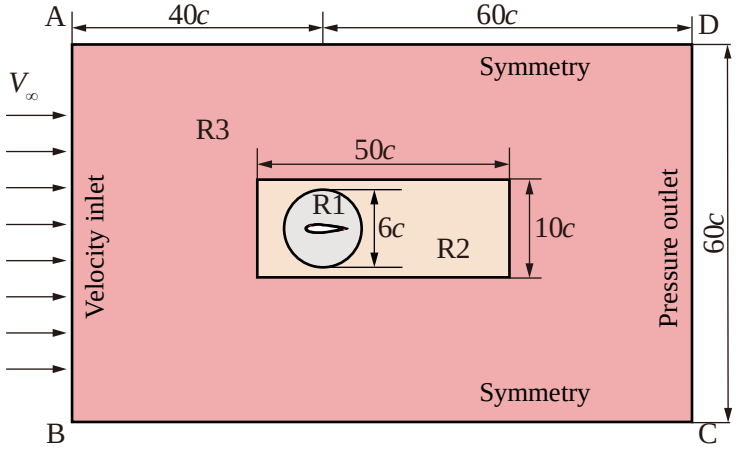

(a) Topology and Boundary Conditions

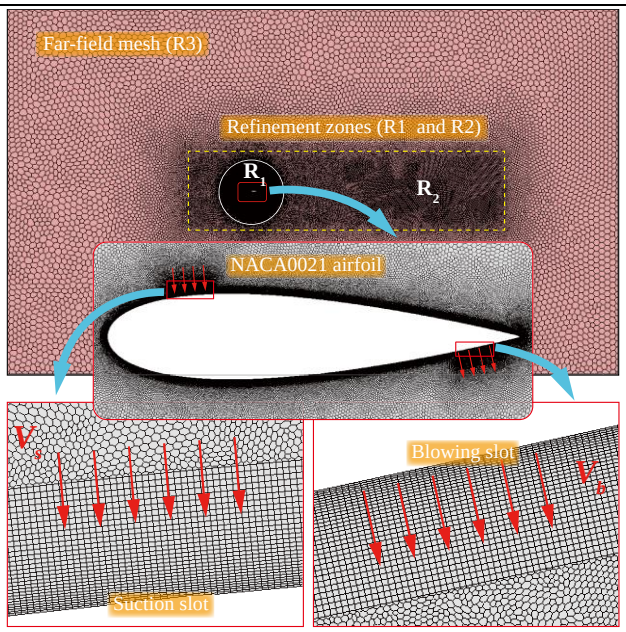

(b) Mesh distribution

Fig. 9 The computational domain of NACA0021 airfoil

Fig. 9b shows the mesh distribution near the airfoil, and its enlarged view shows a close-up of the mesh near the suction and blowing location, respectively. The polygonal cell is adopted to fill the simulation domain, and a boundary layer mesh is used on the airfoil wall. To ensure that the y^+ value is less than 1 for accurate calculation of the viscous bottom layer, the first grid height of the airfoil wall surface is 0.01 mm and the total thickness of the boundary layer is 2.5 mm with a growth ratio of 1.15. The boundary layer mesh is also used for the blowing and suction slots for accurate calculation of the shear flow, and the blowing and suction slots and their two sides are refined accordingly to obtain accurate results.

In this study, the grid distribution of BSS airfoil is the same as baseline configuration to reduce the calculation error. Five different grid scale were used to perform a grid sensitivity study for airfoil with and without BSS (Table 2).

Table 2 The grid distribution of BSS airfoil and smooth configuration

Grid name	Grid refinement level (mm)		Cells
	Airfoil surface (Except for the BSS region)	BSS region (Suction and blowing location)	
G1	0.60	0.15	76258
G2	0.40	0.12	100668
G3	0.28	0.08	142844
G4	0.20	0.05	200459
G5	0.15	0.02	267709

Fig. 10 shows that the lift coefficient tends to stabilize when the grid number of the smooth airfoil exceeds 14 W, while the BSS airfoil requires at least 20W grids for the lift coefficient to ramain unchanged. To ensure the accuracy and efficiency of the simulation, the mesh model G4 was used for the static airfoil calculation.

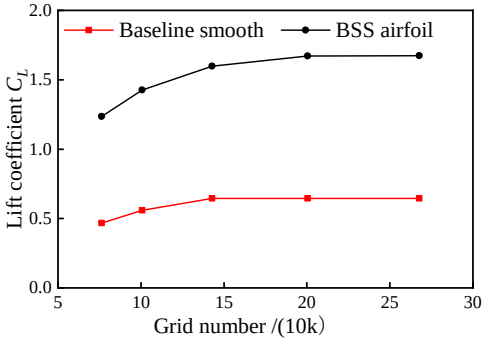

Fig. 10 Lift coefficients of BSS airfoil and smooth configuration for different grid scales.

3.1.2. Validation of numerical method

The comparison of the lift and drag coefficients of the static baseline airfoil against experiment results [62] is illustrated in Fig. 11. The authors of Ref. [62] tested the static and dynamic aerodynamic performance of the NACA0021 airfoil using the Herman-Föttinger-Institute's laminar wind tunnel.

In Fig. 11, for small AOA (α < 7°), the curves basically overlap with the experimental values. While at large AOA, the calculated results are slightly outside the error range. This is due to the occurrence of deep stall at large AOA, which is very sensitive to experimental conditions, and the large uncertainty in the measured data [63]. In addition, turbulence models also have unavoidable errors in the numerical calculations. Notwithstanding, the static stall AOA (α = 14°) obtained from the calculated results is only about 2° higher than the experimental value (α = 12°), and the average relative error between the numerically calculated drag coefficients and the experimental results is less than 7%. Overall, the numerical results meet the requirements of analytical accuracy.

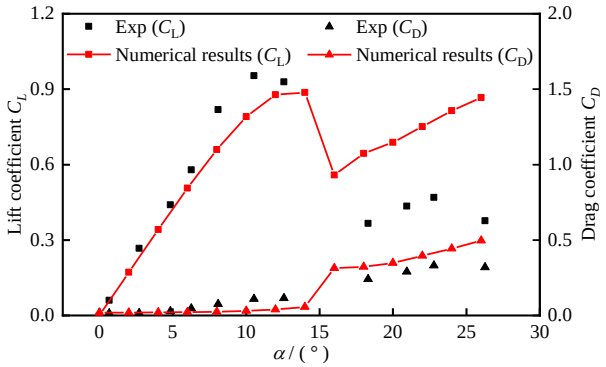

Fig. 11 The comparsion of calculated data with experiment results for static airfoil

3.2. Full three-bladed Darrieus turbine

3.2.1. Grid sensitivity analysis

To simulate the rotation of the turbine, the computational domain (Fig. 12) is divided into a rotating core with a diameter of 1.5 times the turbine diameter D and a fixed domain (40D length × 30D width) surrounding the rotating core. The interface between the rotating core and the fixed domain is a non-conformal with sliding grid to allow the rotation.

The blowing and suction are arranged symmetrically on the inner and outer sides of VAWT blades. As can be seen from Fig. 12, The $(S_{in} - B_{out})$ represents suction in inner side and blowing in outer side, while $(S_{out} - B_{in})$ represents suction in outer side and blowing in inner side. Detailed definitions and different combinations of BSS design are discussed in Section 4.2.

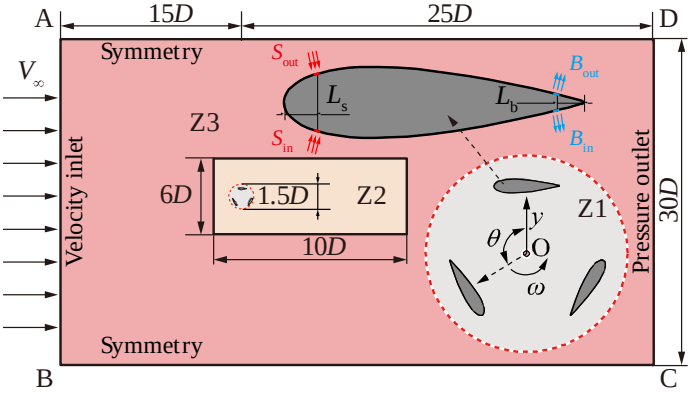

(a) Topology and Boundary Conditions

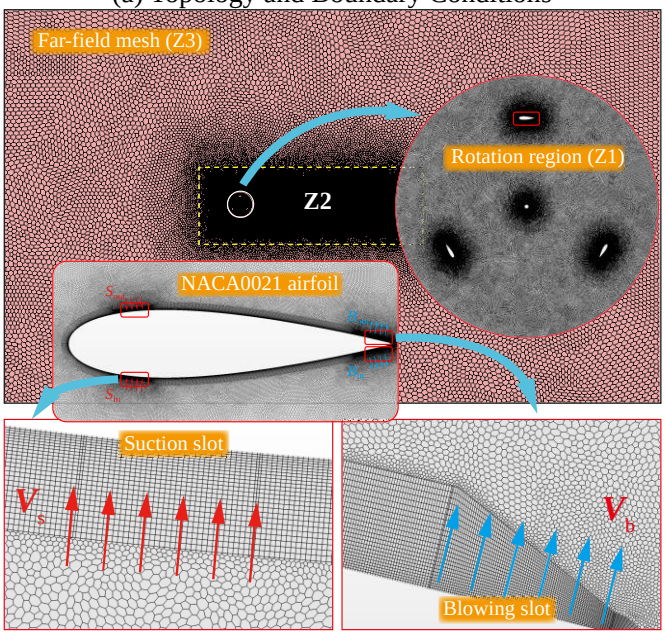

(b) Mesh distribution

Fig. 12 The computational domain of VAWT

The grid sensitivity study for the full-three bladed VAWT is performed at three TSR (λ=1.68, 2.51, and 3.30). The six different grid scales are described in Table 3.

Table 3 The grid distribution of VAWT with or without BSS

Grid name	Grid refinement level (mm)		Cells
	Airfoil surface (Except for the BSS region)	BSS region (Suction and blowing location)	
G1	2.0	1.5	232646
G2	1.2	1.2	336562
G3	0.6	1.0	404202
G4	0.4	0.8	546064
G5	0.2	0.5	790006
G6	0.1	0.2	1087825

The power coefficient curves of smooth and BSS VAWT for six different grids are shown in Fig. 13. At TSR of 1.68, which represents the deep dynamic stall of low TSR, the results of BSS configuration tend to converge when the number of grids increases to G5, and the relative error of C_p between G5 and G6 is 0.26% (<1%). For other cases, only the G4 met the converge requirement. Therefore, the G5 grid number is adopted considering the balance of accuracy and computational cost.

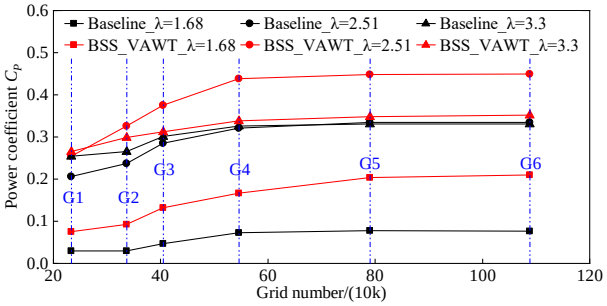

Fig. 13 Power coefficient of smooth and BSS VAWT for six different grids

3.2.2. Revolution convergence analysis

To obtain a steady flow field for data sampling, the wind turbine needs to rotate through a certain number of revolutions to ensure convergence. Calculations are performed for 20 revolutions of the turbine. The behavior of power coefficients and tangential force of single blade is shown in Fig. 14. The TSR of 1.68 represents the flow state with a deep dynamic stall caused by the large variation in AOA, while the TSR of 3.30 represents a more stable flow field at high TSRs. As expected, the tangential force profile corresponding to TSR = 1.68 is characterized by continuous oscillations between positive and negative values due to the high irregularity of the flow field. The case of TSR = 3.30 is much more regular, with a positive upwind peak followed by a flat downwind trend.

For both TSRs, the variation of curves is very large during the first 10 revolutions of the turbine where data sampling leads to a significant overestimation of the turbine performance. A plateau zone was observed as the power coefficient and tangential force approached their limiting values, at approximately 18 revolutions. At this point, the difference between the values at 15 and 18 revolutions was less than 1.5%. Based on this sensitivity analysis, 18 revolutions of the turbine were considered sufficient to guarantee a statically stable converged state. Subsequently, data sampling was performed for 18 revolutions of the turbine. The instantaneous values presented in this paper correspond to the average values of the last three revolutions (revolutions 18-20). Data sampling was performed after 18 revolutions of the turbine to ensure a converged result.

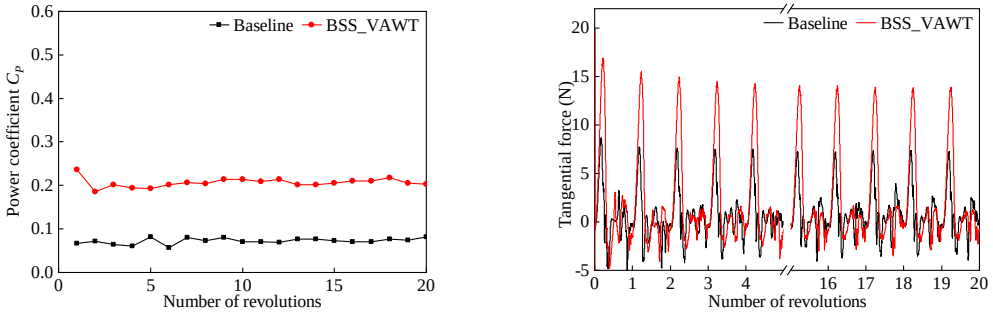

（a）λ=1.68

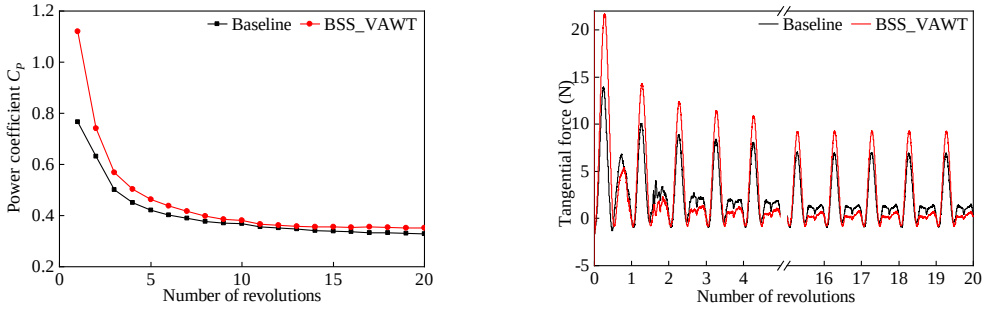

（b）λ=3.30

Fig. 14 Time history of power and tangential force curves for Revolution convergence analysis

3.2.3. Azimuthal increment sensitivity analysis

In the URANS simulation of VAWT, a reasonable choice of time step is required to accurately capture the complex flow structure of the wind turbine. In this study, three time steps are chosen, corresponding to 0.1°, 0.25° and 0.5° azimuthal increment of the wind turbine blade, namely $d\theta_1 = \pi/(360\omega)$, $d\theta_2 = \pi/(720\omega)$, and $d\theta_3 = \pi/(1800\omega)$. The instantaneous torque profile versus azimuth angle for the three different azimuthal increments are shown in Fig. 15. The results at 0.5° significantly overestimate torque, whereas the trends of 0.1° and 0.25° are consistent. The relative change in the average torque of $d\theta_2$ and $d\theta_3$ during a complete revolution will be negligible with a relative error of less than 1%. Therefore, $d\theta_2$ is chosen as the time step for transient calculation of VAWT, after balancing the computational cost and accuracy.

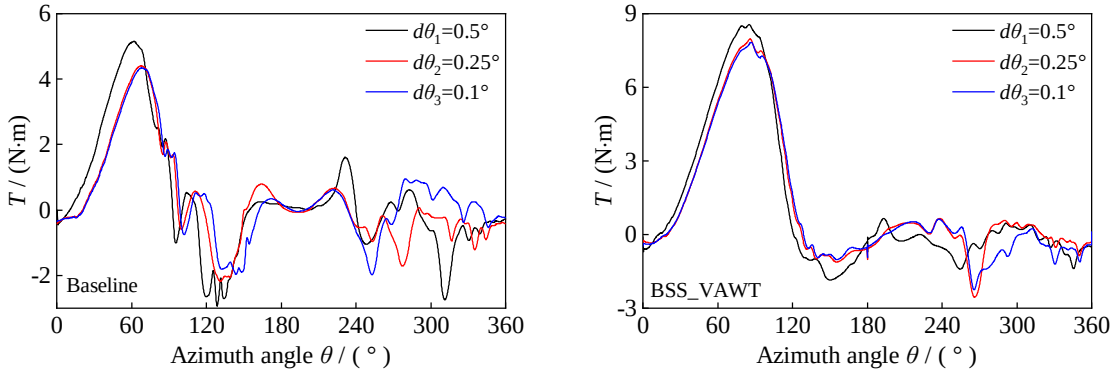

（a）λ=1.68

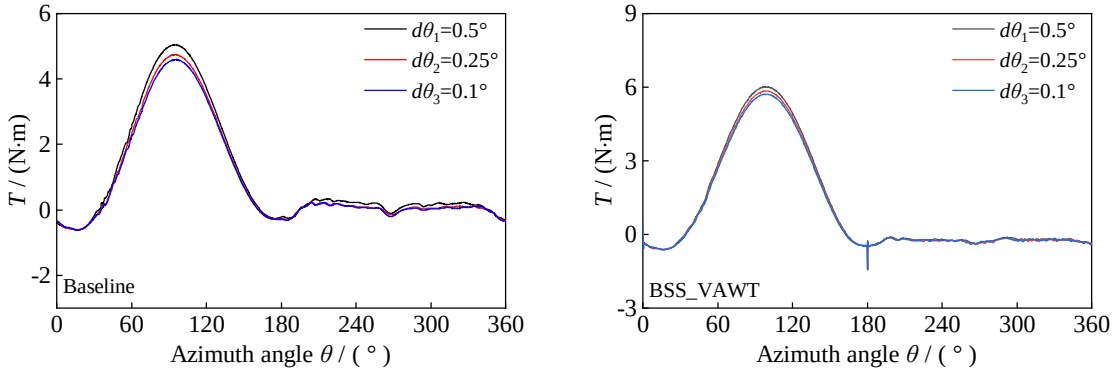

（c）λ=3.30

Fig. 15 Instantaneous torque profile of baseline and BSS VAWT during last revolution at different TSR

3.2.4. Validation using literature results

To verify the reliability of the CFD numerical model, the calculated results were compared with experimental data from Castelli et al. [48]. The same rotor tests were performed in the "Politecnico di Milano" in Milan - Bovisa low turbulence wind tunnel with a test section size of 4000 × 3840 mm. A comparison between the present numerical results, the experimental values, and other published literatures under similar computational conditions is illustrated in Fig. 16.

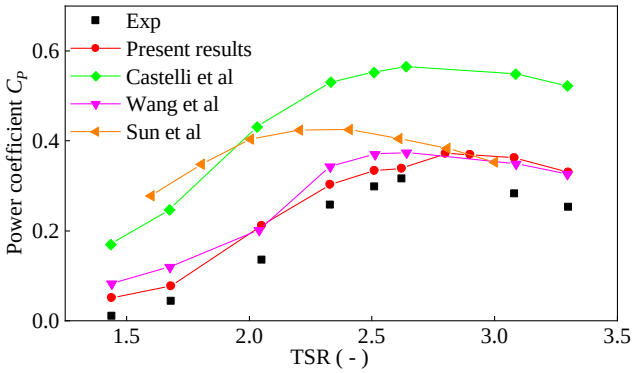

Fig 16 The comparsion of calculated data with literature results and experiment values for VAWT

It is observed that Sun et al [64] using one equation turbulence model (Spalart-Allmaras, S-A) produced large discrepancy relative to experimental data, especially at low to medium TSRs. The two-equation realizable *k-ε* model used by Castelli et al. [48], although capable of replicating the shape of the experimental curve and capturing the optimal TSR, overestimate the C_p values over the whole TSRs even 3-D numerical simulations were employed. This may be caused by the poor quality of the generated mesh, large azimuthal increment, and the low order residual convergence criteria. The average power coefficients predicted by the S-A and *k-ε* turbulence models produce approximately 200% and 230% discrepancies in low to medium TSRs, respectively. In contrast, the SST *k-ω* model adopted by Wang et al. [65] can reduce the corresponding discrepancies to about 150% and 180%. As described in Wilcox [66], the SST *k-ω* model can predict flow separation more accurately than the *k-ε* model in flows with low *Re* numbers.

In comparison with the SST *k-ω* model, these discrepancies can be further reduced by the IDDES model adopted in the presented study, but give similar discrepancy relative to experimental data in higher TSRs (about 20%). The ability of IDDES model to reduce the discrepancy in low and medium ranges of TSRs is contributed by its capability to predict stronger dynamic stall, trailing edge roll up and secondary vortices. The possible explanations for the observed deviation between the current CFD results and the experimental data are extensively discussed in Ref. [50].

3.2.5. Model accuracy

Evaluation of three URANS turbulence models (S-A, *k-ε*, and SST *k-ω*) and a hybrid RANS-LES model (IDDES) for predicting three-blade VAWT performance is discussed above and compared with the experiment of Castelli et al. [48].

Note that, the 2-D formulation of the IDDES turbulence model adopted in this study is inferior to the 3-D formulation since the latter can simulate the three-dimensionality of the separated vortex structure [67]. These small-scale 3-D vortex structures have a crucial effect on the energy dissipation and thus on the pressure and velocity distributions in the flow field. although 2-D IDDES model shows superiorities to 2-D RANS models, the C_p values are overestimated in the whole range of TSRs. Four reasons are supposed to contribute to these discrepancies: (i) The connecting rods and support structures in Fig 7 were ignored in the 2-D CFD modeling. The presence of the struts has a blocking effect on the airflow and the acceleration of the airflow near the struts increases the vortex momentum, which enhances the turbulence mixing and transportation [53]. (ii) A 2-D model represents the VAWT with infinite blade height and span, thus the blockage ratio of the turbine is significantly overestimated [68]. As a result, the effective incoming velocity is much larger than the defined inlet velocity V_∞= 9m/s, which will eventually lead to a large calculated torque and power coefficient. (iii) The 2-D simulation cannot accurately capture the wake profiles, and the 2-D model tends to overestimate the stream-wise velocity in the near wake and underestimate in the far wake [69]. The inherent characteristics of the 2-D model results larger velocity deficit at large downstream distance, which is not conducive to wake recovery. (iv) The 2-D model cannot simulate the flow motions in the spanwise direction of the blade and the evolution of the tip vortices, which play a crucial role in the development of wake aerodynamics [70]. The free-stream flows coming into the wake and the strong vortex motions induced by the blade tip contribute to turbulent mixing and entrainment, thus facilitating wake recovery.

Even though the SST *k-ω* based IDDES model produces more accurate results than other evaluated models, the URANS model is still the preferred choice for the overall performance evaluation of VAWT. This is because the hybrid RANS-LES model has a longer simulation time and more complex grid generation procedure (According to Syawitri et al. [71], the simulation time of the IDDES model is about seven times longer than that of the SST k-*ω* model on the same rotor test and high-performance Intel processor). However, if the analysis is performed to study the flow behaviour such as noise propagation or wake development, it is recommended to use the hybrid RANS-LES turbulence model.

4. Results and discussion

In this section, the operating factors are first analyzed and optimized by an orthogonal experimental design (OED) method based on the effectiveness of the validation work. Subsequently, three different BSS control strategies are proposed, mainly focused on the azimuthal excitation range for a better adaptation to the periodic dynamic stall characteristics of VAWT. Finally, the physical mechanisms of power enhancement and noise reduction for VAWT with BSS control are deeply explored.

4.1. Performance of NACA0021 static airfoil in orthogonal array

Orthogonality is an important index of the OED method, which reflects the independence among design variables. The OED allows sampling across multiple parameter combinations, thus simplifying the optimization process by using only a small number of experiments to assess the importance and independence of each parameter.

4.1.1. Analysis of the OED results

The main parameters affecting the BSS impact include blowing and suction velocity (V_b and V_s), blowing

553 and suction slot width (W_b and W_s) and blowing and suction slot position(L_b and L_s). The velocity and slot
554 width are equivalent to the dimensionless parameter jet momentum coefficient C_μ. As a result, this research
555 balances the range of variables and convergence requirements and divides every parameter into 3 levels (Table 4).
556 The design levels and ranges of the design variables are chosen to cover wide range of configurations. However,
557 considering the regularity of the grid and the convergence of the simulations, these levels are limited to an
558 acceptable range.

559 Table 4 Design parameters and design levels of the BSS.

Parameters	Factor A L_s (mm)	Factor B L_b (mm)	Factor C C_μ (-)
1	0.1 *c*	0 *c*	0.002
2	0.2 *c*	0.05 *c*	0.005
3	0.3 *c*	0.1 *c*	0.01

560 The $L_9(3^4)$ orthogonal array is adopted for the samples design and used in this research (Table 5). Since the
561 main focus of this study is to investigate the BSS impact on the performance of VAWT, a wide range of AOA
562 (0~26°) was applied for all simulations. In Table 5, $\overline{\Delta K_e}$ are the key indexes used to evaluate the aerodynamic
563 performance of NACA0021 airfoil. This represents the average difference in LDR values for airfoils with and
564 without BSS over a range AOA (0-26°) at 2° intervals.

565 Table 5 The OED method in simulation design

Exp No.	Factor A	Factor B	Factor C	$\overline{\Delta K_e}$
1	1	1	1	16.316
2	1	2	2	15.168
3	1	3	3	26.662
4	2	2	3	20.773
5	2	1	2	24.998
6	2	3	1	13.936
7	3	2	1	18.418
8	3	3	2	12.908
9	3	1	3	20.14
K_1	58.146	61.454	48.670	
K_2	59.707	54.359	53.074	
K_3	51.466	53.506	67.575	
$k_1 = K_1/3$	19.382	20.485	16.223	—
$k_2 = K_2/3$	19.902	18.120	17.691	
$k_3 = K_3/3$	17.155	17.835	22.525	
R(ŋ)	2.747	2.649	6.302	

Optimal solution: A2B1C3

Factor ordered by significance (from most to least): C3A2B1

566 The right side of the experimental matrix is the corresponding measured $\overline{\Delta K_e}$ values for the 9 experiments.
567 The matrix of k_i data was obtained by averaging $\overline{\Delta K_e}$ data. For example, the k_2 =19.902 value for Factor A
568 (shown in grey in Table 5) is obtained by adding all $\overline{\Delta K_e}$ values for which Factor A = 2, divided by the total
569 number of values 3, as per Eq. 15:

$$k_3 = (20.773+24.998+13.936)/3 = K_3/3=19.902 \quad (15)$$

The R value of each factor is obtained by calculating the maximum and minimum of k_i. For example, for Factor A: R_A=19.902−17.155=2.747. Obviously, the R value of factor C in the third column is the largest compared to other factors. It is concluded that the change of factor C_μ has the greatest influence on the test index $\overline{\Delta K_e}$. According to R values, the other two factors were ranked from most to least significant, and the order is shown in Table 5. The larger the R value, the greater the impact on the results [72]. The order of influence for R is $R_C > R_A > R_B$. From Table 5, it can be concluded that for factor A, $k_2 > k_1 > k_3$, factor B, $k_1 > k_2 > k_3$, and factor C, $k_3 > k_2 > k_1$. Therefore, the optimum combination of factors will be C3A2B1.

4.1.2. Optimal operation

By comparing the lift and drag coefficient curves of smooth configuration and airfoils with BSS_Opt (Fig. 17), it is observed that BSS_Opt significantly increases the airfoil lift coefficient at different AOA, even at 0°. The stall AOA is delayed from 14°to 24°in comparison with smooth airfoil. The maximum lift coefficient of BSS_Opt airfoil appears at AOA of 22° which is 1.66 times higher than that of the smooth airfoil ($C_{L\max}$ =0.89). In Fig. 17b, the drag coefficient for the smooth airfoil shows a step increase after 14° AOA due to flow separation, while the BSS_Opt airfoil shows no significant change until 24°.

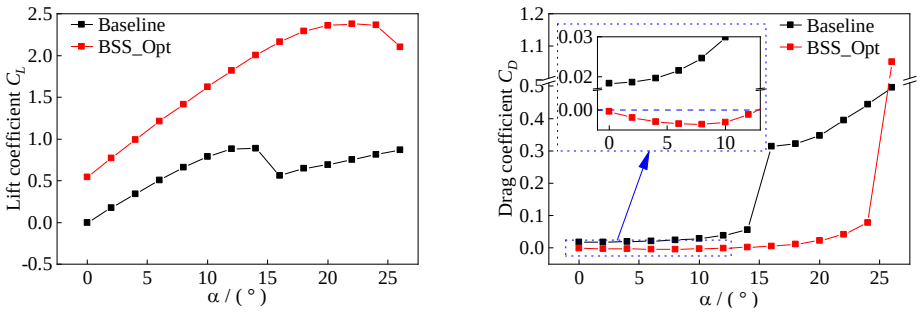

（a）Lift coefficient　　（b）drag coefficient

Fig. 17 Impact of BSS_Opt on the lift and drag coefficients (Re=1×10^6)

To reveal the mechanism of BSS, Fig. 18 presents the streamlines and contours of the streamwise vorticity at α=0°, 12° and 24°. For comparison, two clear scenarios are reported to illustrate the separation location distribution.

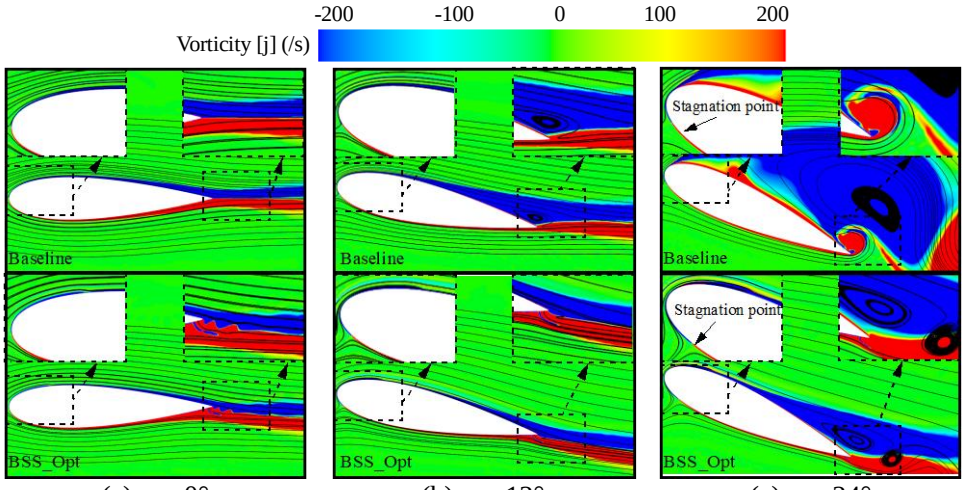

(a) α = 0°　　(b) α = 12°　　(c) α = 24°

Fig. 18 Streamlines and contours of the streamwise vorticity for smooth airfoil and BSS_Opt airfoil

In Fig. 18, the baseline airfoil is in attached flow state at α=0°. In contrast, the BSS_Opt airfoil has an

increased curvature of the nearby streamline due to suction at the leading edge. In addition, the strong shearing effect of the blowing at trailing edge causes the airflow to wash down, thus producing a strong blocking effect at the trailing edge of the pressure surface. This increases the pressure difference between the upper and lower surfaces of the airfoil. In other words, because of the effect of this mechanism, BSS changes the kutta condition of the trailing edge for the smooth airfoil resulting in an increase in effective camber. This reasonably explains why BSS_ Opt enhances the lift coefficient at α=0°.

As the AOA further increases to 12°, flow separation at the trailing edge of the baseline airfoil remarkably intensifies and the separation point substantially moves forward. Under the positive effect of BSS_Opt, the flow reattaches on the airfoil surface. It should be noted that the main contribution at this point comes from the trailing edge blowing at the pressure side of airfoil. This is analogous to a conventional trailing edge GF device [73], thus enhancing the capability of viscous flow attaching on the surface.

As shown in Fig. 18c, when the AOA increased to 24°, the suction surface flow is completely separated, and the counterclockwise vortex at the trailing edge of the airfoil gradually becomes larger. The BSS has a great influence on the aerodynamic characteristics of the airfoil. On the one hand, leading-edge suction can effectively remove the low momentum fluid to inhibit the formation and development of leading-edge vortices, avoid the accumulation of small vortices into large vortices, and eventually reduce the separation area. On the other hand, trailing edge blowing increases the effect by shifting the separation location towards the trailing edge.

4.2. Aerodynamic performance assessment for VAWT

In subsection 4.1, the optimal BSS parameters obtained from the OED results were found to significantly improve the aerodynamic performance of the airfoil. Their effectiveness on VAWT was evaluated.

It is noted that the pressure and suction sides of the VAWT blades alternately switch, which is determined by whether the blades are in the upwind or downwind region. In other words, when the blade rotates to the upwind area, its outer side acts as the pressure side and the inner side as the suction side. The opposite condition was observed as the blade is in the downwind zone. Therefore, if the BSS arrangement applicable to the stationary airfoil is directly employed for the VAWT, harmful effects will inevitably occur in certain azimuthal ranges. For this reason, three different BSS control strategies are proposed in this research to achieve a better energy acquisition efficiency of the VAWT, as shown in Fig. 19.

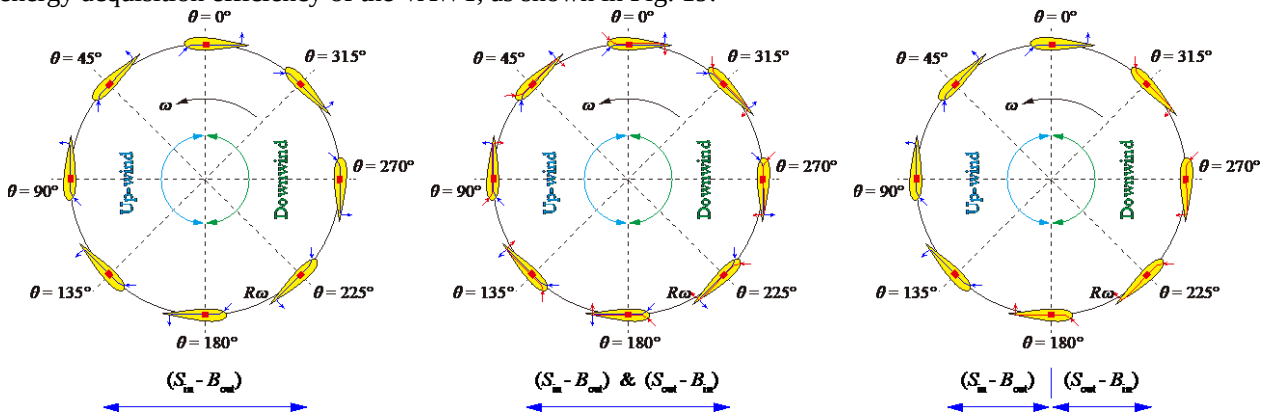

(a) BSS1 (b) BSS2 (c) BSS3

Fig. 19 Different BSS control strategies and the excitation interval of them.

In Fig. 19, the $(S_{\text{in}} - B_{\text{out}})$ represents the suction in inner side and blowing in outer side, while $(S_{\text{out}} - B_{\text{in}})$ represents suction in outer side and blowing in inner side. Accordingly, BSS1 indicates that the $(S_{\text{in}} - B_{\text{out}})$ is activated continuously in a whole rotation cycle while the $(S_{\text{out}} - B_{\text{in}})$ is closed. BSS2 indicates that both the $(S_{\text{in}} - B_{\text{out}})$ and $(S_{\text{out}} - B_{\text{in}})$ work in the whole azimuth range. Particularly, BSS3 represents that

$(S_{in} - B_{out})$ and $(S_{out} - B_{in})$ work in turn during the rotation of the wind turbine. Table 6 detailed the working azimuth angle of BSS1-3.

Table 6 Strategies of BSS action control

Control solution	Working azimuth range $(S_{in} - B_{out})$	Working azimuth range $(S_{out} - B_{in})$
BSS1	0 - 360°	—
BSS2	0 - 360°	0 - 360°
BSS3	0 - 180°	180 - 360°

4.2.1. Loads and moments

Fig. 20 presents the power coefficient of the various BSS control solutions as a function of the TSR. All BSS cases were effective in improving the energy extraction of VAWT, especially at low to medium TSR. It is apparent that the BSS arrangement gives rise to a remarkable improvement of the performance at λ = 1.68 and 2.05. When the TSR is higher than 2.51, BSS3 deployment offers the most effective solution with a noticeable enhancement in the C_p. In contrast, BSS2 and BSS3 arrangements turn out to be equivalent to each other and are represented by almost identically superimposed points.

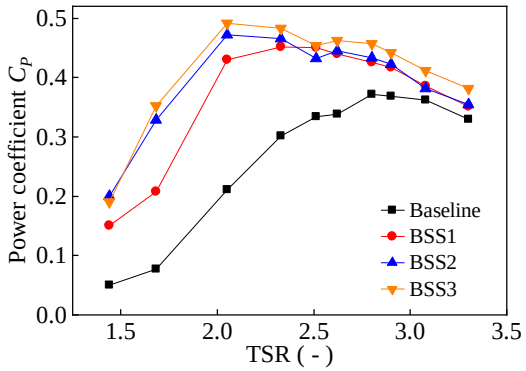

Fig. 20 Power coefficients for VAWT with different BSS control

In addition, the deployment of BSS on the VAWT can shift the peak of power extraction capability backwards to lower TSRs. At TSR of 2.05, BSS3 significantly improved the power coefficients of VAWT and reached the peak value of 0.4923, which are 32.16%, 8.96% and 4.28% higher than the baseline configuration (0.3725), BSS1 (0.4518) and BSS2 (0.4721) respectively. Similarly, the VAWT with BSS control has a lower rotation speed at the same input wind speed, thus reducing the blade centrifugal force and improving the stability and safety of the wind turbine.

To further clarify the mechanism of power augmentation induced by BSS control, the tangential force on single blade and torque profiles for the three-bladed rotor over the last complete revolution are reported in Figs. 21 and 22.

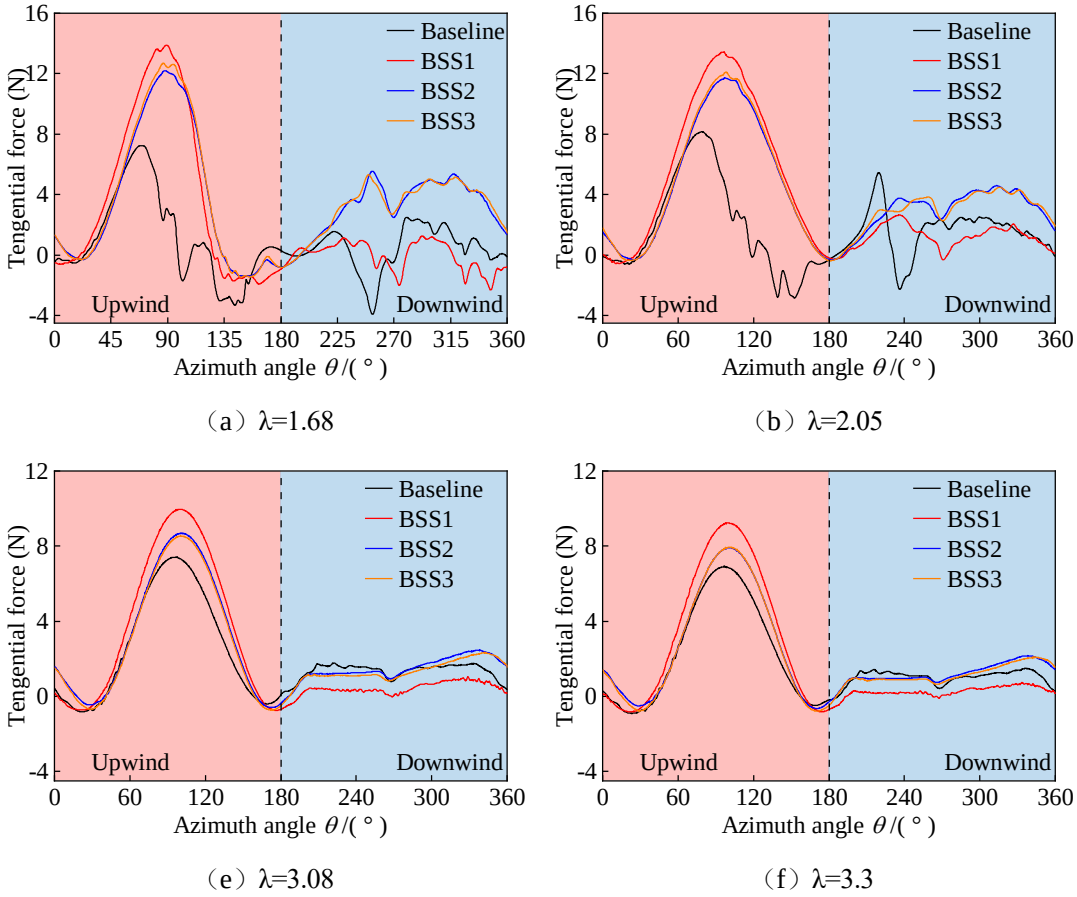

（a）λ=1.68　（b）λ=2.05

（e）λ=3.08　（f）λ=3.3

Fig. 21 The instantaneous tangential force of single blade for VAWT at different TSR

In Fig. 21, the tangential force provided by the smooth rotor is quite poor and characterized by a sharp fluctuation trend at λ = 1.68 and 2.05, with a negative thrust between 90° and 150°, as well as between 240° and 360°. The boosting effect of the BSS control is evident and ensures excellent behaviour through the whole azimuth region is achieved.

Conversely, the higher TSRs have a much more regular curves, with a positive upwind peak followed by a downwind flat trend. In particular, when this solution is compared to the baseline case and BSS2-3, BSS1 shows a significantly higher efficiency within the upwind half, although this is entirely outweighed by the lower downwind power extraction. It can be explained that the BSS1 overly boosts the upwind extraction, which is then compensated with a resistant torque along the downwind half.

These observations are also confirmed by Fig. 22, as expected. Because of the high irregularity that affects the flow field at low TSRs, the torque profile corresponding to λ = 1.68 and 2.05 is characterized by continuous oscillations between positive and negative values. As discussed in previous studies [74], this irregularity occurs because, at low TSRs, the AOA variation is so large that the airfoil experiences deep stall with significant drop in performance. Furthermore, the BSS control can completely eliminate negative torque and prevent the wind rotor from bearing excessive alternating loads. This will eventually improve the energy efficiency and prolongs the service life.

With further increase in TSR, the lifting effect of BSS 1-3 on the torque coefficient of the whole rotor is weakened, and the change law basically remains the same.

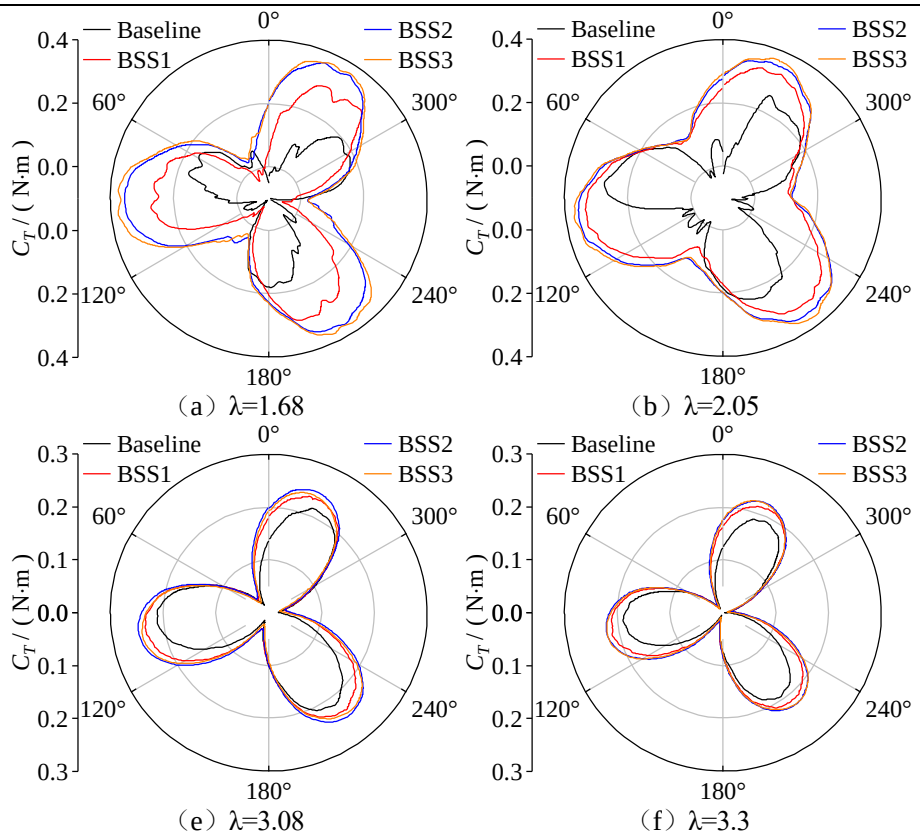

Fig. 22 The load fluctuation versus azimuth angle of VAWT

4.2.2. Flow pattern and wake analysis

To gain a batter insight into the physical reasons which led to these results, a detailed analysis of the flow field corresponding to a TSR of 1.68 was carried out. These observations are shown in Fig. 23, where the vorticity contours are reported for the baseline configuration and different BSS control solutions at the azimuthal position of 60-150° and 240-330°.

As shown in Fig. 23, the baseline configuration is in a deep stall at 90-150° azimuth, and there is a wide range of flow separation region, with periodic vortex shedding on the inner side of the blade. This causes the deterioration of energy extraction. Conversely, the opposite happens for the BSS cases, which mainly due to the "double effect" produced by the good combination of suction and blowing jet. On the one hand, the leading-edge suction can remove the low momentum fluid and replace it with fresh high-energy fluid. This enhances the fluid′s ability to resist the inverse pressure gradient, thus effectively inhibiting the formation and development of leading-edge vortices. On the other hand, the trailing edge blowing can increase the virtual curvature of the airfoil, leading to the reduction of the effective AOA. This induces the airflow to leave the trailing edge of the airfoil in a downwash tendency, which eventually suppresses the roll-up phenomenon of trailing edge vortices.

Moving forward to azimuth angle of 240-330°, vortex shedding appears on the outer side of the blade for the baseline configuration and is significantly influenced by the wake disturbance in the upwind region, which is most evident at azimuth angle of 240°. The interaction of these vortices within the downwind blades contributes to the high variability of the torque profile, as mentioned above. However, the wake vortices of the BSS cases dissipate much quicker than for the smooth one to reduce the frequency and intensity of the shedding disturbance. Comparing the three BSS cases, although BSS1 has a good flow separation control effect in the upwind area, it has little effect in the downwind region. This is because in the downwind zone, the flow separation occurs outside the blade (see Fig. 23b), while BSS1 is also blowing on the outer side of the blade. This is not conducive to the attachment of the flow. This phenomenon is observed in existing PFC strategies such as Dimple [75] and

GF [13] (simulated with the same rotor). The former is installed on the inner side of the VAWT blades to trap the vortices, which is only applicable to weak flow separation conditions, and introduces structural drag in the downwind region. The latter is mounted on the outside of the blade and functions in similar manner to the outward blowing jet of BSS1. This significantly improves the dynamic stall occurring on the upwind side, but with almost no gain in the downwind region.

Remarkably, BSS2 and BSS3 achieve almost the same gain over the whole azimuthal range. This confirms that the force curves and torque profile in the above analysis are identical. In contrast, the control effect of BSS3 is better than that of BSS2. As can be seen from Fig. 23 (c) and (d), the vortex wake is shorter and smaller, especially at the azimuth angle of 90°, 120° and 330°, 270°. This is mainly because the blowing and suction for BSS2 are activated simultaneously on both sides of the blade, and the $(S_{\text{out}} - B_{\text{in}})$ in the upwind area and $(S_{\text{in}} - B_{\text{out}})$ in the downwind region increase the flow resistance and play the opposite role. However, BSS3 will eliminate the adverse effects by alternately blowing and suction in the upwind and downwind region. More specifically, the blowing jet of the BSS3 is similar to the switching GF [76], which can adjust its position according to the flow conditions to the extent that it retracts into the blade when necessary, thereby minimizing the drag caused by the GF in the downwind region. The difference is that the suction control in the BSS3 strategy can further enhance the blowing effect and the proposed active device does not change the airfoil shape, thus highlighting the superiority.

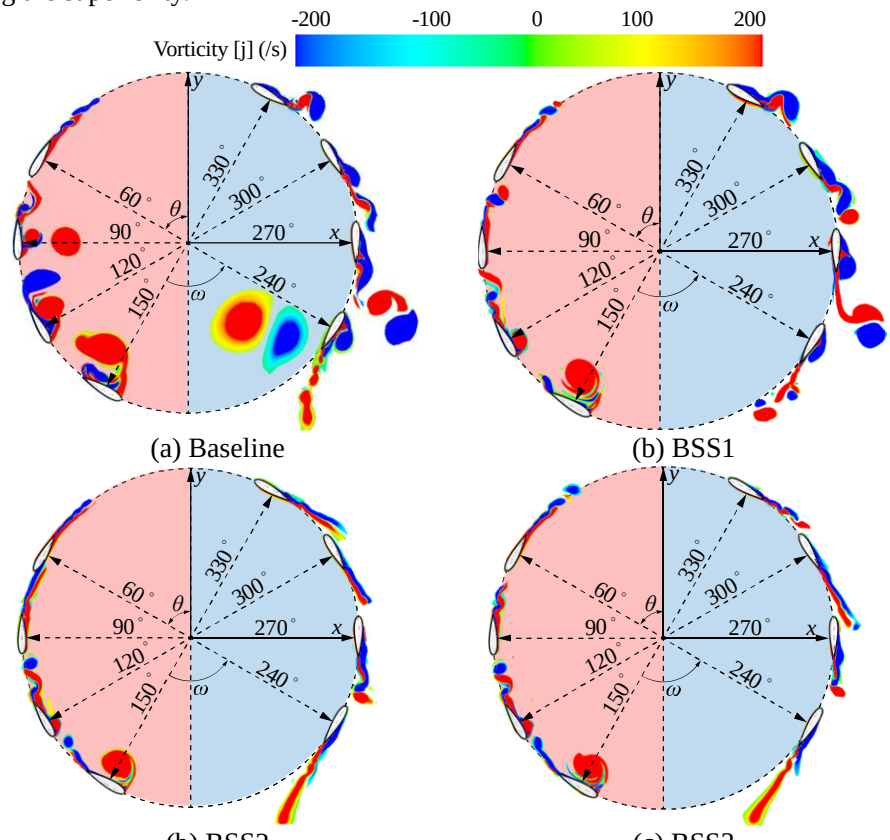

Fig. 23 Vorticity contours around both side of blade at different azimuth positions.

To investigate the impact of the BSS strategies on the wake distribution for VAWT, the wake velocity contours for baseline and BSS 1-3 were compared at TSR of 1.68 and 2.51, as shown in Fig 24.

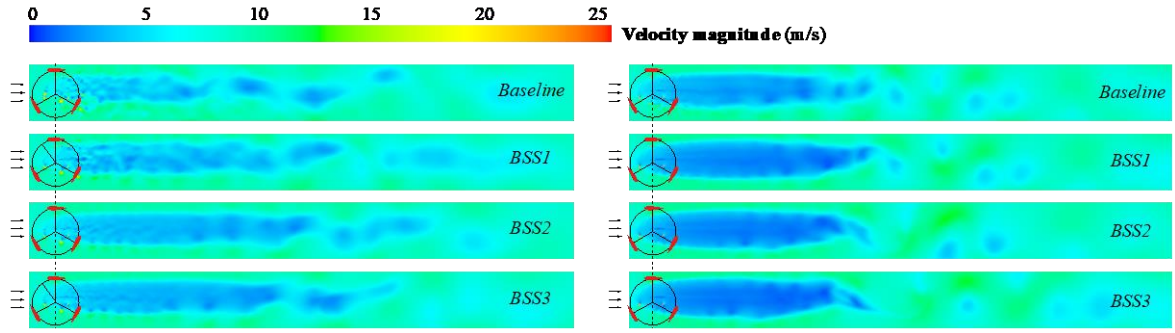

（a）λ=1.68　　（b）λ=2.51

Fig. 24 Velocity magnitude for wake analysis at different TSRs

In Fig. 24, the wake of the BSS cases is longer and wider than that of the baseline configuration at low TSR. This is because BSS 1-3 suppresses flow separation, which in turn allows the VAWT to absorb more wind energy from the incoming flow. This increases the wake deficit and reduces the wake recovery rate. It can be explained that the above phenomenon is in accordance with the law of energy conservation, which states that the greater the extraction in the upwind area, the lower the energy content of the downwind flow. As the TSR increase to 2.51, the wake length becomes almost identical to all cases. The BSS cases show a slight increase in low-speed region and wake width region, indicating that the effect of BSS on the wake distribution is not obvious at high TSR.

Further quantification of the velocity distribution for VAWT wake is illustrated in Fig. 25. This includes sampling line segment length of 2D, located at 5D and 10D downstream of the wind turbine, where the time-averaged velocities are normalized by the free incoming velocity V_{∞}.

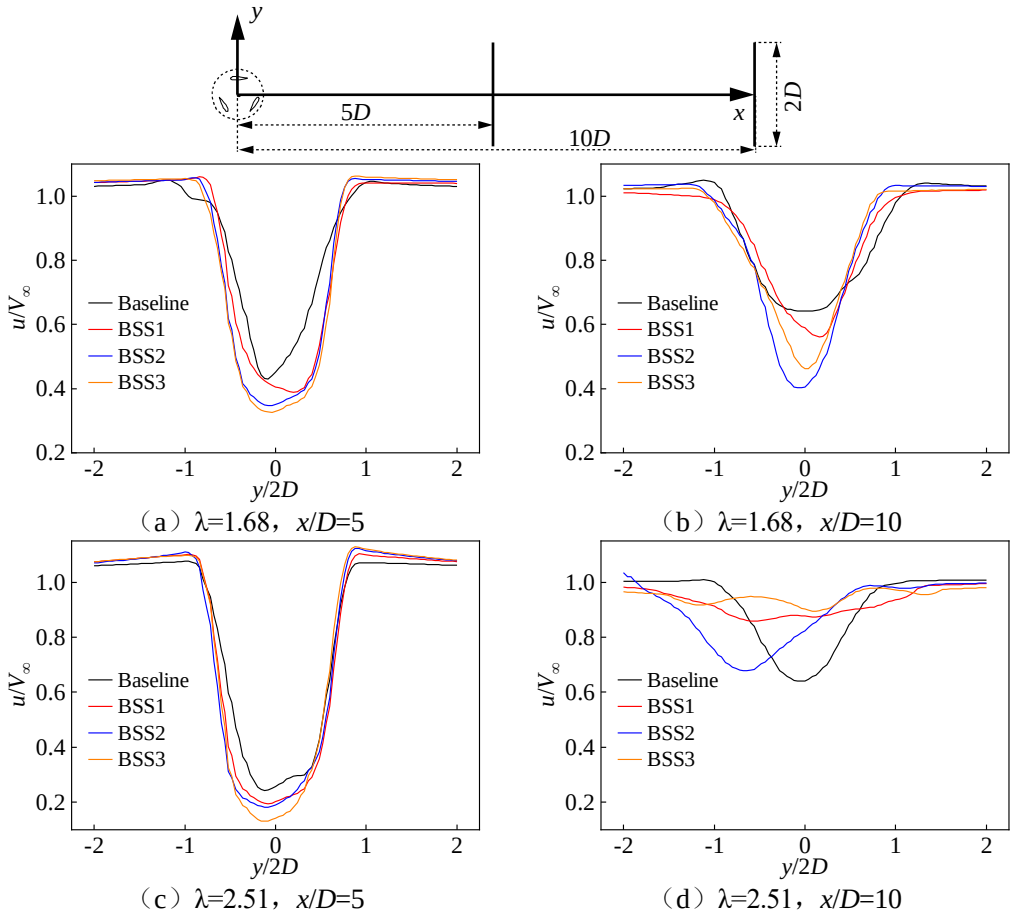

（a）λ=1.68，*x*/*D*=5　　（b）λ=1.68，*x*/*D*=10

（c）λ=2.51，*x*/*D*=5　　（d）λ=2.51，*x*/*D*=10

Fig. 25 Dimensionless time-averaged wake velocity at different TSRs

In Fig. 25, it can be seen that the wake velocity deficit increases for different BSS strategies compared to the baseline VAWT at TSR of 1.68. This is more evident for BSS2 and BSS3, indicating that the BSS design takes longer to recover from the incoming wind speed effects. At *x*/*D*=5, the minimum values of the dimensionless wake velocities of BSS1~3 are 0.39, 0.35 and 0.33, which are 9.30%, 18.60% and 23.26% lower than the respective baseline configuration (0.43). The energy extraction of VAWT is greatly improved at this time, which is consistent with the velocity contours in the above analysis. As the TSR increases to 2.51, the effect of BSS1-3 on VAWT aerodynamic performance gain decreases, thus reducing the wake deficit, and allowing the wake velocity to gradually recover from the incoming flow velocity at x/D=10.

Therefore, if this active control is to be used in a wind farm arrangement, the layout of VAWTs should be properly considered. The downstream wind turbines should be located far from the upstream wind turbines, or the wind turbines should be staggered to maximize energy utilization.

4.2.3. The power requirement for the active device

In this section, the energy requirements and net benefits of the BSS design proposed in this research are presented. A critical consideration for the BSS design is whether it can generate sufficient power to cover the energy consumption it produces to justify the economics of its application. Therefore, an Aerodynamic Figure of Merit (AFM) [77] is introduced to evaluate the performance of BSS control solutions, and it is defined as Eq. (16):

$$\mathrm{AFM} = \frac{P_{Controlled} - P_{BSS}}{P_{Baseline}} \tag{16}$$

where $P_{Controlled}$ is the output power for the VAWT with the BSS control, P_{BSS} is the input power required for BSS, $P_{Baseline}$ is the output power for baseline VAWT.

Table 7 presents the energy consumption of different BSS strategies, the power produced by the turbine with this active control, and the corresponding AFM values at different operating conditions.

At low TSR, different BSS strategies showed excellent performance, particularly at TSR of 1.44. The AFM values of BSS1-3 are 2.96, 2.88 and 4.02, which represents increase in the net wind turbine output by 2.96, 2.88 and 4.02 times, respectively. Furthermore, it is observed that increasing the TSR increases the energy consumption required for BSS. Although both BSS2 and BSS3 significantly enhance the power extraction compared to BSS1 from the above load and torque analysis results, the net benefits of BSS2 are much less than those of BSS3. It should be noted that zero benefit was recorded at the highest TSR (namely, $\lambda = 3.30$). The reason for this observation is that the blowing and suction for BSS2 design work simultaneously on both sides of the blade over the entire azimuth range, thus leading a dramatic increase in power consumption. Therefore, from an engineering point of view, intermittent excitation is recommended.

In summary, BSS3 has a positive net gain over the entire range of TSRs and is an economically active flow control method for SB-VAWT.

Table 7 The cost-effectiveness analysis for BSS control solutions at different TSR.

λ	P_{clean}	BSS1			BSS2			BSS3		
		P_{BSS} (W)	$P_{Controlled}$ (W)	AFM	P_{BSS} (W)	$P_{Controlled}$ (W)	AFM	P_{BSS} (W)	$P_{Controlled}$ (W)	AFM
1.44	23.38	5.19	74.41	2.96	7.13	99.26	2.88	5.19	93.24	4.02
1.68	35.56	6.33	102.25	2.70	10.04	161.26	2.59	6.63	168.90	4.35
2.05	97.36	7.86	205.72	2.03	11.50	228.64	1.99	8.85	235.24	2.26
2.33	139.12	9.24	217.03	1.49	14.15	228.25	1.46	10.53	233.00	1.56
2.51	153.80	10.44	217.95	1.35	15.98	215.06	1.31	11.52	220.51	1.32
2.62	155.79	11.16	213.77	1.30	17.77	222.47	1.26	12.39	225.23	1.35
2.80	171.31	13.02	208.94	1.14	20.47	219.82	1.10	13.74	224.01	1.20
2.90	169.80	13.95	206.17	1.13	21.92	216.41	1.09	14.43	218.08	1.19
3.08	166.81	15.63	193.08	1.06	24.41	199.85	1.01	15.54	205.10	1.10
3.30	151.91	17.79	179.71	1.07	28.08	191.44	1.00	17.25	192.67	1.15

4.3. Aeroacoustics performance assessment for VAWT

Since the control solution of BSS3 is comparatively better in terms of power production and energy consumption than the BSS2 and BSS3 design, only the impact of BSS3 on the noise characteristics of the VAWT is discussed and compared with the baseline configuration in this section.

The radiation pattern of aeroacoustic noise is mainly determined by the pressure fluctuations and the noise generation and propagation in the fluid flow. This can be accurately calculated when the aerodynamic results such as power and torque profile were validated within allowable error [78]. In Section 3, the computational parameters including the revolutions, grid sensitivity and azimuthal increment have been carefully discussed and verified though comparison with experimental values. Thus, the noise is predicted using these flow field calculations and the noise reduction mechanism is analyzed in this section.

The unsteady flow problem is solved by the SST $k-\omega$ based IDDES turbulence model and the far-field noise is predicted by using the FW-H acoustics integral formulation. Calculations are performed for 23

revolutions of the turbine. The first 20 revolutions are used for stabilization and convergence of the flow field, and the flow characteristics are obtained by averaging the results during the last three revolutions (21-23), which is also used to calculate the acoustic signal for all receivers (Fig 26). Rec. 1, Rec. 2, Rec. 3 and Rec. 4 (marked in red) are arranged to capture the wake noise propagation, while the monitoring points distributed along the circumference of the rotor (marked in yellow) are used to predict the directional distribution of the VAWT.

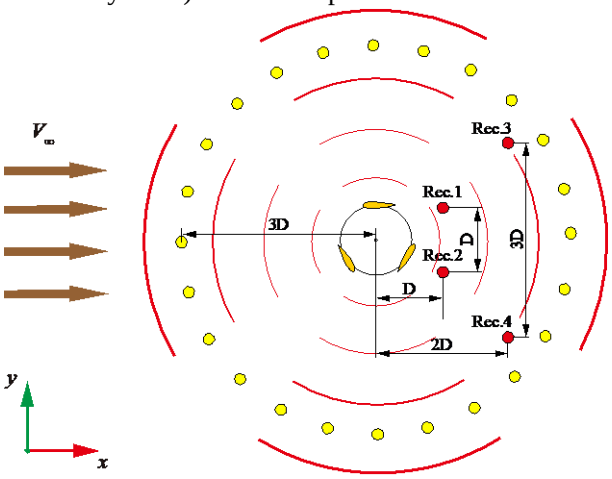

Fig. 26 The distribution of noise receiving point

4.3.1. Sound pressure spectra

The time-based acoustic pressure data obtained in the last three revolutions was analyzed in the frequency domain through Fast Fourier Transform (FFT). The noise spectrum of monitoring points (Rec.1-4) at different TSR is shown in Fig. 27.

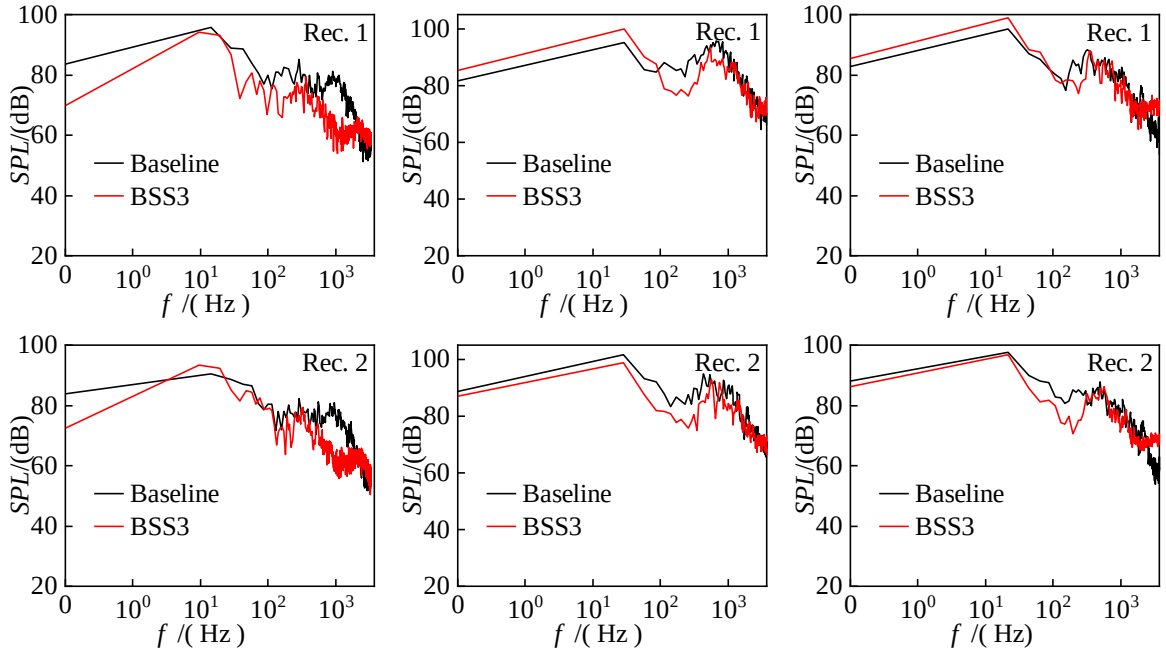

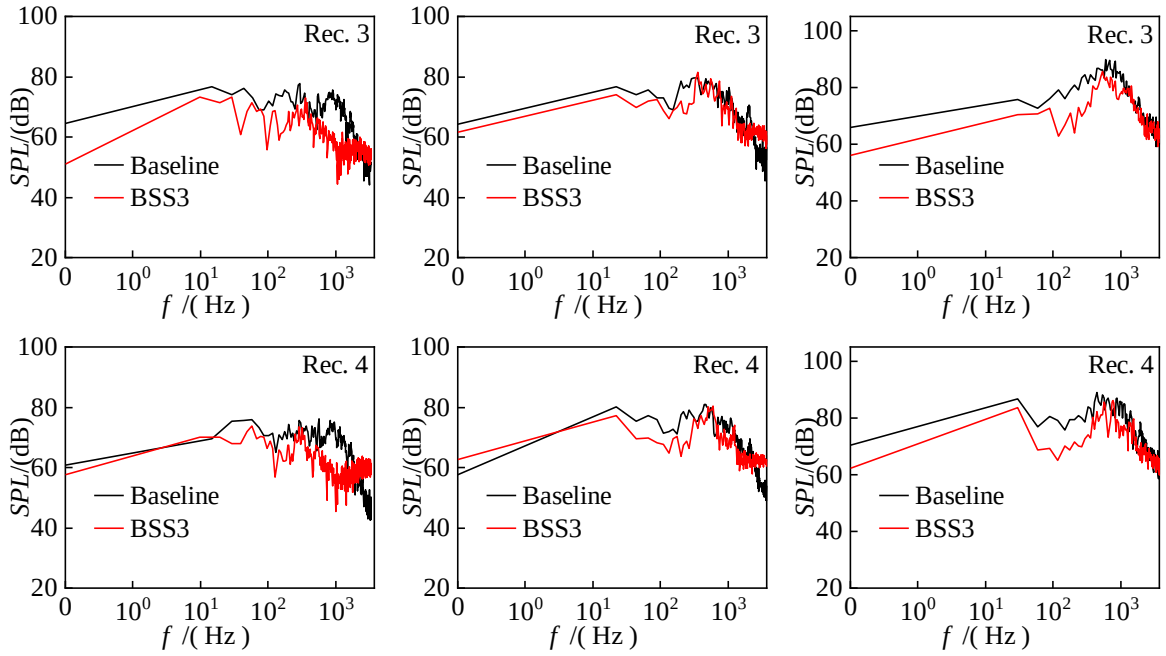

（a）λ=1.68　　（c）λ=2.51　　（b）λ=3.30

Fig. 27 Sound pressure level spectra of Rec. 1-4 at different TSR

It is observed that as the monitoring points are located far from the wind turbine, and the sound pressure levels gradually decay. This is due to the dissipation of pressure pulsations during propagation, resulting in higher noise spectral levels in Rec. 3 and Rec. 4 than Rec. 1 and Rec. 2 over the whole frequency range. In addition, the noise from a VAWT increases with the increase of TSR, which consistent with phenomenon reported by Mohamed et al. [6]. From an engineering viewpoint, the rotational speed should be lower for it to reduce the noise generation. Based on the aerodynamic results in Section 5.1, it is concluded that BSS3 can reduce the optimal TSR as expected. This means that the VAWT with BSS has a lower rotational speed at the same incoming flow conditions, further demonstrating the merits of BSS.

At low TSR, the baseline VAWT experiences deep dynamic stall and vortices are periodically shed from the blade surface. The BSS3 design can effectively control the flow separation in the whole azimuth range, thus significantly reduce the radiated noise. With further increase of TSR, Rec. 1 represents a lower noise level at high frequencies and conversely, a higher noise level at low frequencies. This may be due to Rec. 1 being more susceptible to trailing edge shedding vortices than Rec. 2 when the blades are rotated though an azimuth angle of 360° (0°). It should be noted that the reduction in average noise level at high frequencies is greater than the increase in average noise at low frequencies for Rec. 1, which eventually weakened the noise components. Furthermore, most of the receivers present the same results with 80% noise spectrum lower than the baseline configuration. Particularly, all receivers for BSS3 design have lower noise levels in the frequency range of 100-1000Hz.

4.3.2. Directivity of sound pressure

Fig. 28 illustrates the directionality of sound pressure at different TSR for baseline configuration and BSS3 design. The 24 additional monitoring points are arranged around the wind rotor at a distance of 3D to calculate the overall sound pressure level (OSPL). According to the time-based pressure fluctuation dates, the OSPL can be defined by Eqs. (17) and (18):

$$\mathrm{OSPL} = 20\log_{10}\left[\frac{p'_{rms}}{p_{ref}}\right] \tag{17}$$

$$p'_{rms} = \sqrt{\frac{1}{\Delta T}\int_{T_1}^{T_2} p^2 \cdot dt} \tag{18}$$

where P_{ref} is the reference acoustic pressure (P_{ref} =2×10^5 Pa), p'_{rms} is the effective sound pressure, calculated by taking the root mean square of the instantaneous sound pressure over a certain time interval.

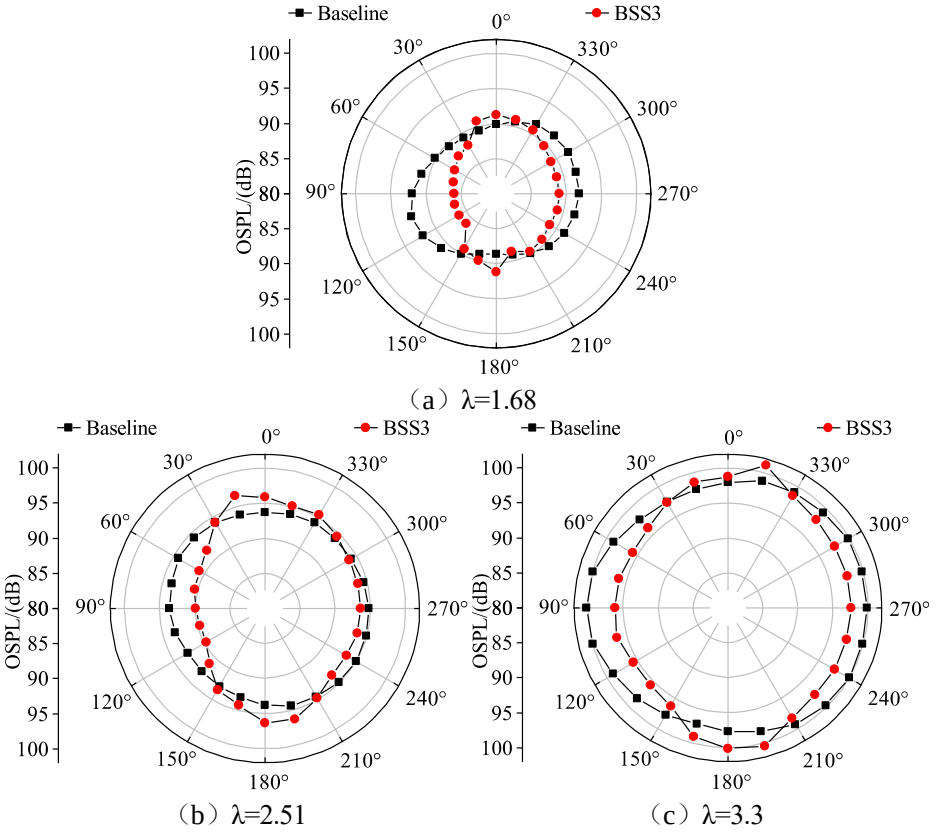

（a）λ=1.68　（b）λ=2.51　（c）λ=3.3

Fig. 28 The directivity distribution of noise propagation at different TSR

In Fig. 28, it is first observed that the propagation of VAWT noise along the circumferential direction increases with increase in the TSR, which is consistent with the previous results. Conversely, at all TSRs, the receivers located in the vertical direction of BSS3 design experience higher noise level, approximately 2-3dB louder than for the baseline configuration. The reason is that (S_{in}, B_{out}) and (S_{out}, B_{in}) switch frequently at azimuth angles of 0° and 180° during the rotation of the VAWT, resulting in no obvious contribution to the performance enhancement, even deteriorating the stability of the flow field.

Notwithstanding, the OSPL is significantly reduced in the horizontal direction. More specifically, the proposed BSS3 configuration weakens the noise propagation in both upwind and downwind regions. The minimum value of OSPL for BSS3 is approximately 85.93 dB at θ=105° for λ=1.68, 89.88 dB at θ=180° for λ=2.51, and 96.14 dB at θ=180° for λ=3.3, which decrease the noise by 6.56 dB, 3.67 dB and 4.09 dB, respectively compared to the baseline configuration at the same monitoring location.

4.3.3. Noise reduction mechanism

To further investigate the physical mechanism of the noise reduction induced by the BSS3 design. Fig. 29 presents the pressure fluctuations for the variation of TSR at monitoring points Rec. 1, Rec. 2, Rec. 3 and Rec. 4.

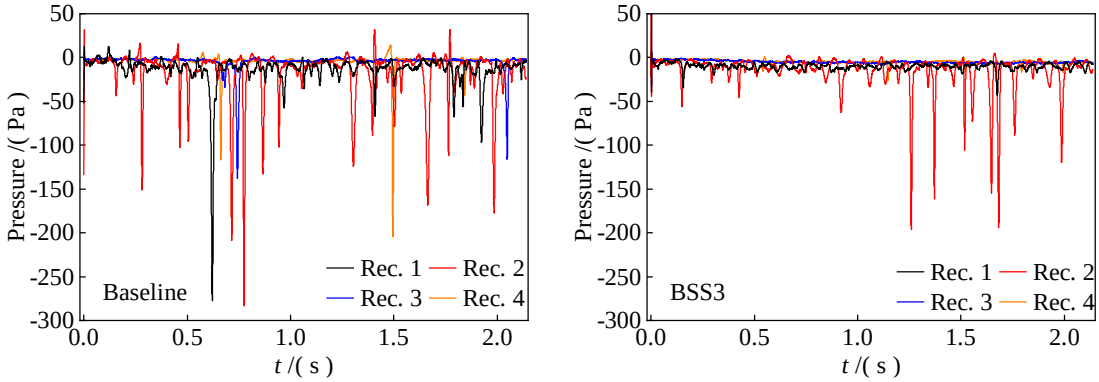

（a）λ=1.68

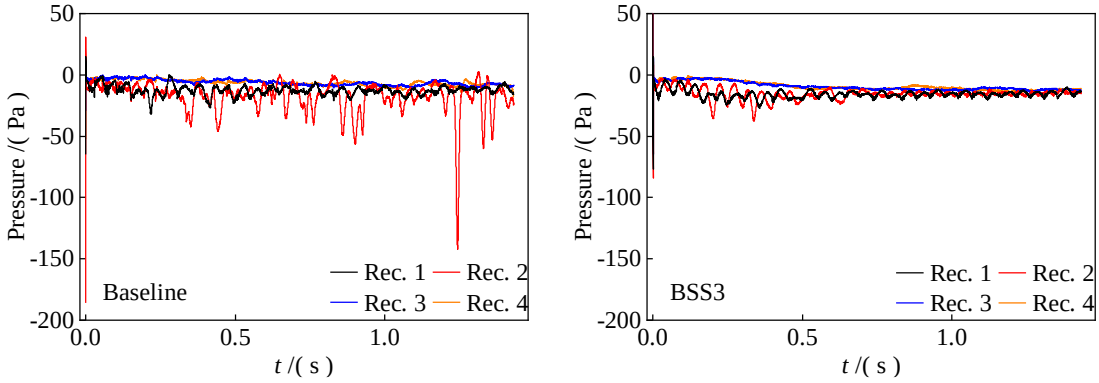

（b）λ=2.51

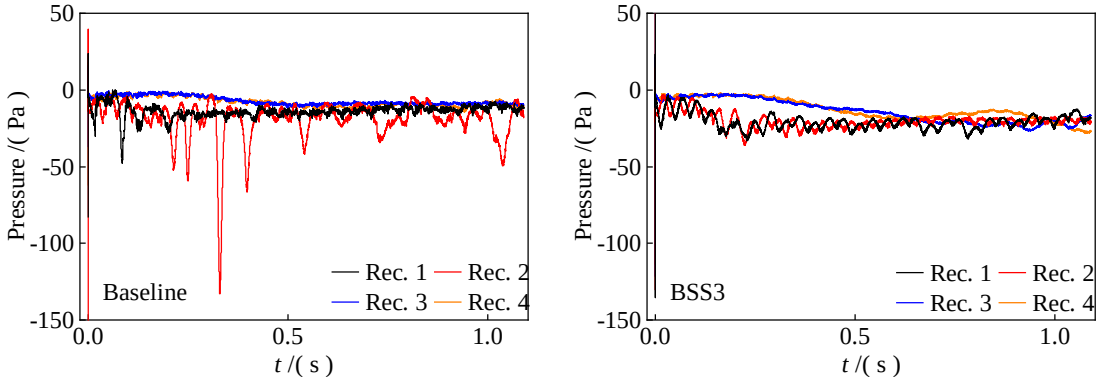

（c）λ=3.3

Fig. 29 Comparison of pressure fluctuations for baseline and BSS3 configuration at different TSR

In Fig. 29, the sound pressure of the smooth VAWT varies greatly in the range of -300 to -50 Pa at TSR of 1.68. The plot shows a similar trend at higher TSR, while the sound pressure for the BSS3 design has relatively small oscillation in comparison with the baseline configuration. In conjunction with Fig. 23, improving the flow field is a critical requirement for noise reduction, as the pressure variation in the flow field is closely related to the magnitude of the vortex shedding.

Finally, it is observed that the proposed BSS3 design can significantly enhance the energy extraction for VAWT at different TSRs and reduce the size of vortex shedding in upwind and downward regions, which generates more stable pressure fluctuations in the flow field. Consequently, the BSS design is suitable from two perspectives: performance enhancement and noise reduction.

5. Conclusions

In view of the complex flow field characteristics of VAWT, a blowing-suction synergy active control strategy was constructed and implemented on airfoil and VAWT to investigate the aerodynamic and aeroacoustic

characteristics of the VAWT.

The main conclusions from this study are summarized as follows：

1. A preliminary assessment of the effect of BSS on static airfoil was conducted to evaluate the BSS parameters by OED method including suction position relative to leading-edge (L_s), blowing position relative to trailing-edge (L_b) and jet coefficient (C_μ). The OED results indicate that the lift and drag characteristics of NACA0021 airfoil are significantly affected by C_μ and more sensitive to L_s , while weakly influenced by L_b . The optimal combination is C_μ =0.01, L_s =0.2*c* and L_b =0*c*.

2. The optimal BSS enhances the aerodynamic performance of airfoil, whose peak lift coefficient was increased by 166% in comparison to the baseline configuration. Furthermore, the static stall angle is delayed to about 24° and influenced by the application of BSS.

3. The “double effect” produced by the good combination of suction and blowing-based jets offers the key to improving the aerodynamic performance of an airfoil and VAWT. The leading-edge suction can remove the low momentum fluid, effectively inhibiting the formation and development of the leading-edge vortex and enhancing the ability of the fluid to resist the inverse pressure gradient. On the other hand, trailing edge blowing can virtually increase the camber of the airfoil, so that the airflow leaves the trailing edge of the airfoil in a downwash trend, thus significantly suppressing the trailing vortex roll-up phenomenon.

4. The BSS significantly enhances the energy extraction at low to medium TSR, and even have a noticeable contribution at higher TSR. In addition, the BSS also reduces the optimal TSR to 2.33, alleviate the dynamic stall phenomenon and eliminate the negative tangential force at whole azimuth angle. This reduces the blade centrifugal force and increases the stability and safety of the wind turbine.

5. The flow field of VAWT is effectively improved due to the addition of the BSS. By inhibiting flow separation and reducing the size and frequency of vortex shedding, the BSS significantly reduces the scope of the separation zone. This dissipates the blade tail vortex more rapidly when the blade is in the upwind region. This eventually reduces the amount and intensity of the upstream vortex shedding that will interfere with the blade as it rotates towards the downwind region.

6. Optimal arrangement of the BSS configuration on VAWT provides a noticeable increase in aerodynamic performance. More specifically, the power coefficients of VAWT reach the peak value of 0.4923 at TSR=2.05, which is 32.16%, 8.96% and 4.28% higher than the respective baseline configuration (0.3725), BSS1 (0.4518) and BSS2 (0.4721).

7. The BSS reduces the VAWT noise by moderating pressure fluctuation, stabilizing the flow field and influencing the vortex shedding characteristics. The optimal BSS control solution is found to modify the SPL spectra at frequencies between about 100 and 1000 Hz and reduce the noise levels of wind turbine by up to 6.56 dB.

In practical engineering applications, the air pump inside a blade should be added with a valve to divert the airflow between alternate blowing and suction cycles. In addition, it is recommended that the suction and blowing directions should be perpendicular to the blade surface to ensure a good geometical profile of airfoil.

Future work should focus on the effects of BSS on self-starting performance of the VAWT. In the current study, the instantaneous torque curves of VAWT were strongly shifted upwards at low TSR, which verifies that the rotor benefits from the self-start at lower wind speed.

Acknowledgement

The authors would like to acknowledge the support of National Natural Science Foundation (NSFC) of China in 2020, through the multi-objective optimization, including the geometric, material and structural parameters,

with a view to forming a design theory by combining load reduction characteristics, aerodynamic efficiency and structural performance for ultra-long flexible blades (Grant No. 52006148) and is grateful for the financial support (NSFC 51976131). The authors wish to acknowledge the support of Professor John Summerscales, University of Plymouth, for his review of the manuscript.

References

[1] Rezaeiha A, Montazeri H, Blocken B. Characterization of aerodynamic performance of vertical axis wind turbines: Impact of operational parameters. Energy Conversion and Management, 2018, 169: 45-77.

[2] Griffith D T, Paquette J, Barone M, Goupee A J, Fowler M J, Bull D, Owens B. A study of rotor and platform design trade-offs for large-scale floating vertical axis wind turbines. Journal of Physics Conference Series, 2016, 753: 102003.

[3] Tjiu W, Marnoto T, Mat S, Ruslan M H, Sopian K. Darrieus vertical axis wind turbine for power generation II: Challenges in HAWT and the opportunity of multi-megawatt Darrieus VAWT development. Renewable Energy, 2015, 75: 560-571.

[4] Miao W P, Li C, Yang Y, Pavesi G, Yang J, Xie X Y. Investigation of wake characteristics of a yawed HAWT and its impacts on the inline downstream wind turbine using unsteady CFD. Journal of Wind Engineering and Industrial Aerodynamics, 2017, 168: 60-71.

[5] Tadamasa A, Zangeneh M. Numerical prediction of wind turbine noise. Renewable Energy, 2011, 36: 1902-1912.

[6] Mohamed M H. Aero-acoustics noise evaluation of H-rotor Darrieus wind turbines. Energy, 2014, 65: 596-604.

[7] Dessoky A, Lutz T, Bangga G, Krämer E. Computational studies on Darrieus VAWT noise mechanisms employing a high order DDES model. Renewable Energy, 2019, 143: 404-425.

[8] Benim A C, Diederich M, Gül F, Oclon G, Taler J. Computational and experimental investigation of the aerodynamics and aeroacoustics of a small wind turbine with quasi-3D optimization. Energy Conversion and Management, 2018, 177: 143-149.

[9] Su J, Lei H, Zhou D, Han Z L, Bao Y, Zhu H B, Zhou L. Aerodynamic noise assessment for a vertical axis wind turbine using Improved Delayed Detached Eddy Simulation. Renewable Energy, 2019, 141: 559-569.

[10] Suarez J M, Flaszynski P, Doerffer P. Application of rod vortex generators for flow separation reduction on wind turbine rotor. Wind Energy, 2018, 21(11): 1202-1215.

[11] Hafie C, Mbarek T B. Reduced order model for the lift coefficient of an airfoil equipped with extrados and/or trailing edge flexible flaps. Computers & Fluids, 2019, 180: 82-95.

[12] Wang H P, Jiang X, Chao Y,Li Q, Li M Z, Zhang W N, Chen T. Effects of leading edge slat on flow separation and aerodynamic performance of wind turbine. Energy, 2019, 182: 988-998.

[13] Bianchini A, Balduzzi F, Rosa D D,Ferrara G. On the use of Gurney Flaps for the aerodynamic performance augmentation of Darrieus wind turbines. Energy Conversion and Management, 2019, 184: 402-415.

[14] Mostapha T, Nachtane M, Boudounit H. Finite Element Analysis of Composite Offshore Wind Turbine Blades under Operating Conditions. Journal of Thermal Science and Engineering Applications, 2018: 1-28.

[15] Prandtl L. Über Flüssigkeitsbewegung bei sehr kleiner Reibung. Verhandl III, Intern. Math. Kongr. Heidelberg, Auch: Gesammelte Abhandlungen, 2, 1904: 484-491.

[16] Karim M A, Acharya M. Suppression of dynamic-stall vortices over pitching airfoils by leading-edge suction. Aiaa Journal, 1994, 32(8): 1647-1655.

[17] Pechlivanoglou, G. Passive and active flow control solutions for wind turbine blades, Technische

Universitaet Berlin, 2013.
[18] Abdullah T A, Jasim L M, Dawood A S. Experimental study of lift/drag ratio enhancement using continuous normal suction. AL-Rafdain Engineering Journal, 2012, 20(1): 76-84.
[19]Lei J M, Liu Q Y, Li T. Suction control of laminar separation bubble over an airfoil at low Reynolds number. Journal of Aerospace Engineering, 2019, 233(1): 81-90.
[20] Rezaeiha A, Montazeri H, Blocken B. Active flow control for power enhancement of vertical axis wind turbines: Leading-edge slot suction. Energy, 2019, 189: 116131.
[21] Sun J J, Huang D G. Numerical investigation of boundary layer suction control positions on airfoils for vertical-axis wind turbine. Journal of Mechanical Science and Technology, 2021(6): 1-12.
[22] Traub L W, Miller A C, Rediniotis O. Comparisons of a gurney and jet flap for hinge-less control. Journal of Aircraft, 2004, 41(2): 420-423.
[23] Traub L W, Agarwal G. Aerodynamic characteristics of a gurney/jet flap at low reynolds numbers. Aircraft 2008, 45(2): 424-429.
[24] Feng L H, Shi T Y, Liu Y G. Lift Enhancement of an Airfoil and an Unmanned Aerial Vehicle by Plasma Gurney Flaps. AIAA Journal, 2017: 1-11.
[25] Fu Y H, Shi J P, Huang D G, Zhang W G. Influence of Continuous Jet at the Lower Surface on Airfoil Aerodynamic Performance. Advances in Guidance, Navigation and Control, 2021, 644: 1745-1753.
[26] Du J, Li Y W, Li Z H, Li J C, Wang Z N, Zhang H W. Performance enhancement of industrial high loaded gas compressor using Coanda jet flap. Energy, 2019, 172: 618-629.
[27] Zhang J, Du J, Zhang M, Chen Z, Zhang H W, Nie C Q. Aerodynamic Performance Improvement of a Highly Loaded Compressor Airfoil with Coanda Jet Flap. Journal of Thermal Science, 2022, 31: 151-162.
[28] Rice T T, Taylor K, Amitay M. Wind tunnel quantification of dynamic stall on an S817 airfoil and its control using synthetic jet actuators. Wind Energy, 2019, 22(1): 21–33
[29] Yen J, Ahmed N A. Enhancing vertical axis wind turbine by dynamic stall control using synthetic jets. Journal of Wind Engineering & Industrial Aerodynamics, 2013, 114: 12–17.
[30] Menon A. Numerical investigation of synthetic jet based flow control for vertical axis wind turbine. Rensselaer Polytechnic Institute,2014.
[31] Zhu H T, Hao W X, Li C, Ding Q W, Wu B H. Application of flow control strategy of blowing, synthetic and plasma jet actuators in vertical axis wind turbines. Aerospace Science and Technology, 2019, 88: 468–480.
[32] Wang P L, Liu Q S, Li C, Miao W P, Luo Shuai, Sun K, Niu K L. Effect of trailing edge dual synthesis jets actuator on aerodynamic characteristics of a straight-bladed vertical axis wind turbine. Energy, 2022, 238: 121792.
[33] Johnson S C, Dam C P V, Berg D E. Active load control techniques for wind turbines. Technical Report No. SAND2008-4809, Sandia National Laboratories, 2008.
[34] Greenblatt D, Schulman M, Ben-Harav A. Vertical axis wind turbine performance enhancement using plasma actuators. Renewable Energy, 2012, 37(1): 345–354.
[35] Greenblatt D, Lautman R. Inboard/outboard plasma actuation on a vertical-axis wind turbine. Renewable Energy, 2015, 83: 1147–1156.
[36] Ma L, Wang X D, Zhu J, Kang S. Dynamic Stall of a Vertical-Axis Wind Turbine and Its Control Using Plasma Actuation. Energies, 2019, 12(19): 1-18.
[37] Dumitrache A, Frunzulica F, Ionescu T C. Mathematical modelling and numerical investigations on the

Coanda effect. Nonlinearity, Bifurcation and Chaos-Theory and Applications, 2012: 101-132.
[38] Jones G S, Joslin R D. Overview of Circulation Control Pneumatic Aerodynamics: Blown Force and Moment Augmentation and Modification as Applied Primarily to Fixed-Wing Aircraft. 2015.
[39] Graham H Z, I V, Hubbell M, Panther C, Wilhelm J, Angle G M II, Smith J E. Circulation controlled airfoil analysis through 360 degrees angle of attack. Proceeding of the ASME 2009 3rd international conference on energy sustainability collocated with the heat transfer and InterPACK09 conferences. San Francisco, California, USA. 2009. 571–577.
[40] Shires A, Kourkoulis V. Application of circulation controlled blades for vertical axis wind turbines. Energies. 2013, 6(8): 3744–3763.
[41] Dano B, Kirk D, Zha G. Experimental Investigation of Jet Mixing Mechanism of Co-Flow Jet Airfoil. Flow Control Conference. 2013.
[42] Xu H Y, Qiao C L, Ye Z Y. Dynamic stall control on the wind turbine airfoil via a co-flow jet. Energies, 2019, 9(6), 1-25.
[43] Liu J Q, Chen R Q, You Y C, Shi Z Y. Numerical investigation of dynamic stall suppression of rotor airfoil via improved co-flow jet. Chinese Journal of Aeronautics, 2022, 35(3): 169-184.
[44] Sun X J, Xu Y Q, Huang D G. Numerical simulation and research on improving aerodynamic performance of vertical axis wind turbine by co-flow jet. Journal of Renewable and Sustainable Energy, 2019, 11, 013303.
[45] Eisele O, Pechlivanoglou G, Nayeri C N, Paschereit C O. Flow control using plasma actuators and the root region of wind turbine blades. In DEWEK 2011. DEWI, 2010.
[46] Liu Q S, Miao W P, Ye Q, Li C. Performance assessment of an innovative Gurney flap for straight-bladed vertical axis wind turbine. Renewable Energy, 2022, 185: 1124-1138.
[47] Castelli M R, Englaro A, Benini E. The Darrieus wind turbine: proposal for a new performance prediction model based on CFD. Energy 2011, 36(8): 4919-4934.
[48] Castelli M R, Ardizzon G, Battisti L, Benini E, Pavesi G. Modeling Strategy and Numerical Validation for a Darrieus Vertical Axis Micro-Wind Turbine. Asme International Mechanical Engineering Congress & Exposition, 2010: 409-418.
[49] Bianchini A, Balduzzi F, Ferrara G, Ferrari L. Virtual incidence effect on rotating airfoils in darrieus wind turbines. Energy Conversion and Management 2016, 111: 329–338.
[50] Rezaeiha A, Kalkman I, Blocken B. Effect of pitch angle on power performance and aerodynamics of a vertical axis wind turbine. Applied Energy, 2017, 197: 132-150.
[51] Li Y, Calisal S M. Three-dimensional effects and arm effects on modeling a vertical axis tidal current turbine. Renewable Energy, 2010, 35: 2325-2334.
[52] Gosselin R, Dumas G, Boudreau M. Parametric study of H-Darrieus vertical-axis turbines using CFD simulations. Journal of Renewable and Sustainable Energy, 2016, 8: 053301.
[53] Rezaeiha A, Kalkman I, Montazeri H, Blocken B. Effect of the shaft on the aerodynamic performance of urban vertical axis wind turbines, Energy Conversion and Managment. 2017, 149: 616-630.
[54] De G M G, De L C G, Ficarella A, Marra F. Comparison between synthetic jets and continuous jets for active flow control: application on a NACA 0015 and a compressor stator cascade. Aerospace Science and Technology, 2015, 43: 256-280.
[55] Daroczy L, Janiga G, Petrasch K, Webner M, Thévenin D. Comparative analysis of turbulence models for the aerodynamic simulation of H-Darrieus rotors. Energy, 2015, 90: 680-690.

[56] Ma N, Lei H, Han Z L, Zhou D, Bao Y, Zhang K, Zhou L, Chen C Y. Airfoil optimization to improve power performance of a high-solidity vertical axis wind turbine at a moderate tip speed ratio. Energy, 2018, 150: 236-252.
[57] Guo Y H, Li X C, Sun L X, Gao Y, Gao Z M, Chen L J. Aerodynamic analysis of a step adjustment method for blade pitch of a VAWT. Journal of Wind Engineering and Industrial Aerodynamics, 2019, 188: 90-101.
[58] Lei H, Zhou D, Bao Y, Li Y, Han Z L. Three-dimensional Improved Delayed Detached Eddy Simulation of a two-bladed vertical axis wind turbine. Energy Conversion and Management, 2017, 133: 235-248.
[59] Menter F R. Two-equation eddy-viscosity turbulence modeling for engineering applications. AIAA Journal, 1994, 32(8), 1598-1605.
[60] Shur M L, Spalart P R, Strelets M K, Travin A K. A hybrid RANS-LES approach with delayed-DES and wall-modelled LES capabilities. International Journal of Heat and Fluid Flow, 2008, 29(6): 1638-1649.
[61] Kinzel M P, Maughmer M D, Duque E. Numerical Investigation on the Aerodynamics of Oscillating Airfoils with Deployable Gurney Flaps. Aiaa AIAA Journal, 2010, 48(7): 1457-1469.
[62] Holst D, Church B, Wegner F, Pechlivanoglou G, Nayeri C N, Paschereit C O. Experimental Analysis of a NACA 0021 Airfoil under dynamic angle of attack variation and low Reynolds numbers. Journal of Engineering for Gas Turbines and Power. 2019, 141(3): 031020.
[63] Gupta S, Leishman J G. Dynamic stall modelling of the S809 aerofoil and comparison with experiments. Wind Energy, 2010, 9(6): 521-547.
[64] Sun X, Wang Y, An Q, Cao Y, Wu G Q, Huang D G. Aerodynamic performance and characteristic of vortex structures for darrieus wind turbine. I. Numerical method and aerodynamic performance. Journal of Renewable and Sustainable Energy, 2014, 6(4): 043134.
[65] Wang Y, Shen S, Li G H, Huang D G, Zheng Z Q. Investigation on aerodynamic performance of vertical axis wind turbine with different series airfoil shapes. Renewable Energy, 2018, 126: 801-818.
[66] Wilcox D C. Turbulence Modelling for CFD, DWC Industries, California, USA, 2006.
[67] Ferreira C J S, Zuijlen A V, Bijl H, Bussel G V, Kuik G V. Simulating dynamic stall in a two-dimensional vertical-axis wind turbine: verification and validation with particle image velocimetry data. Wind Energy, 2010, 13(1): 1-17.
[68] Elsakka M M, Ingham D B, Ma L, Pourkashanian M, Moustafa G M, Elhenawy Y. Response Surface Optimisation of Vertical Axis Wind Turbine at low wind speeds. Energy Reports, 2022, 8: 10868-10880.
[69] Lam H F, Peng H Y. Study of wake characteristics of a vertical axis wind turbine by two and three-dimensional computational fluid dynamics simulations. Renewable Energy, 2016, 90: 386-398.
[70] Franchina N, Persico G, Savini M. 2D-3D Computations of a Vertical Axis Wind Turbine Flow Field: Modeling Issues and Physical Interpretations. Renewable Energy, 2019, 136: 1170-1189.
[71] Syawitri T P, Yao Y F, Chandra B, Yao J. Comparison study of URANS and hybrid RANS-LES models on predicting vertical axis wind turbine performance at low, medium and high tip speed ratio ranges. Renewable Energy. 2021, 168: 247-269.
[72] Comakli K, Simsek F, Comakli O, Sahin B. Determination of optimum working conditions R22 and R404A refrigerant mixtures in heat-pumps using Taguchi method. Apply Energy 2009, 86 (11): 2451–2458.
[73] Zhu H T, Hao W X, Li C, Ding Q W, Wu B H. A critical study on passive flow control techniques for straight-bladed vertical axis wind turbine. Energy, 2018, 165: 12-15.
[74] Wang Z Y, Wang Y C, Zhuang M. Improvement of the aerodynamic performance of vertical axis wind turbines with leading-edge serrations and helical blades using CFD and Taguchi method. Energy

Conversion and Management, 2018, 177: 107-121.
[75] Sobhani E, Ghaffari M, Maghrebi M J. Numerical investigation of dimple effects on darrieus vertical axis wind turbine. Energy, 2017, 133: 231-241.
[76] Chen L, Xu J, Dai R. Numerical prediction of switching gurney flap effects on straight bladed VAWT power performance. Journal of Mechanical Science and Technology, 2020 (34):4933-4940.
[77] Stalnov O, Kribus A, Seifert A. Evaluation of active flow control applied to wind turbine blade section. Journal of Renewable and Sustainable Energy, 2010, 2(6): 063101.
[78] Mo J O, Lee Y H. Numerical simulation for prediction of aerodynamic noise characteristics on a HAWT of NREL phase VI. Journal of Mechanical Science and Technology, 2011, 25(5): 1341-1349.